A systematic methodology to calibrate wellbore failure models, estimate the in-situ stress tensor and evaluate wellbore cross-sectional geometry

Asmae Dahrabou [a,*], Benoît Valley [a], Peter Meier [b], Philip Brunner [a], Andrés Alcolea [b]

[a] *Center for Hydrogeology and Geothermics, University of Neuchâtel, Switzerland*
[b] *Geo-Energie Suisse AG, Zürich, Switzerland*

ARTICLE INFO

ABSTRACT

Deep geothermal boreholes, often drilled to the crystalline basement, suffer from borehole breakouts that compromise borehole stability and/or lead to low drilling performance. These issues increase the cost of deep geothermal projects and lead to irregular cross-sectional geometries that may entangle well completion (e.g., packer isolation for zonal stimulation, cementing, etc.). Thus, the proper knowledge of rock strength, state of stress and their interactions at the closest vicinity of the borehole is key to the success of deep geothermal drilling. Typically, the magnitudes of the vertical and minimum horizontal principal stresses, S_v and S_{hmin}, respectively, can be estimated while S_{Hmax} is difficult to constrain. This paper presents a systematic methodology to jointly evaluate the heterogeneous distributions of the stress tensor principal components and orientations, and the rock strength properties (e.g. cohesion, friction). Model parameters are estimated from measurements available during or shortly after drilling, i.e., breakout width, breakout extent/depth of penetration, breakout orientation and drilling induced tensile fractures. Additionally, measurements of estimated parameters or transformations of them can be considered in the calibration in a generic manner (e.g., S_{hmin} interpreted from XLOT). For illustration purposes, the methodology is applied to the extensive borehole data set along the crystalline section of the borehole BS-1, in Basel (Switzerland). The methodology allows us (1) to derive plausible sets of stress and strength parameters reproducing the complex distribution of breakouts along BS-1, and (2) to unveil the paradox of having no borehole breakouts at sections with high density of natural fractures.

1. Introduction

Deep geothermal boreholes of an Enhanced Geothermal System (EGS) are drilled to hot and low permeable rock masses, most often in the crystalline basement (BS-1 in Basel, Häring et al.[1], Soultz-sous-Forêts site, Rummel and Baumgärtner et al.[2], Habanero well in Australia, Fernández-Ibáñez et al.[3] or Pohang in South-Korea, Alcolea et al.[4], amongst others), to depths between 3000 and 5000 m. Drilling performance, i.e., the first critical factor to the economic success of an EGS, borehole stability and the regularity of the borehole cross-section are controlled by the interplay between rock strength and the state of stress around the borehole. If drilling was successful, a second critical factor to the installation of the EGS is well completion, which most often includes the stimulation of pre-existing fractures. An irregular borehole cross-section involving deeply penetrating borehole breakouts or drilling induced tensile fractures (DITFs) may entangle, or even preclude, the correct placing of packers, whose sealing is mandatory

for a targeted stimulation of pre-existing fractures. This issue becomes critical when stimulating so-called multi-stage EGSs, in which natural fractures are individually isolated with packers and stimulated sequentially. For the aforementioned reasons, the accurate knowledge of the interplay between the local state of stress and the rock strength is crucial to the success of an EGS.

Methods to characterize stresses in deep boreholes are described in the literature[5,6] and can be classified into two groups, namely 1st order and 2nd order methods. 1st order methods aim at estimating linear depth trends, whereas 2nd order methods characterize the perturbations around the trend arising from the presence of faults, fractures or other sources of rock heterogeneity. Due to the dominant effect of gravity on the stress state and the relatively small range of density variations in most rocks, it is common to consider that one principal stress is vertical and to estimate its magnitude, S_v, as the weight of the overburden by integrating the linear trends observed in density logs. The assumption

of a vertical principal stress may not be accurate due to the effects of (1) topography (e.g., at shallow boreholes in hilly zones, Evans and Meier[7]), (2) nearby excavations (e.g., at the monitoring boreholes of a tunnel, Martin et al.[8]), or (3) even due to the drilling of the borehole itself. In a 1st order approximation, the magnitudes of horizontal stress are also approximated by depth linear trends[5]. Hydraulic tests (e.g. XLOTs)[9] can be used to estimate the minimum horizontal principal stress, S_{hmin}. The direction of penetration of borehole breakouts is usually an accurate estimate of the orientation of S_{hmin}. As suggested by, Zoback et al.[5] the geometry of breakouts along the borehole can be used to infer a linear trend of S_{Hmax}.

The aforementioned 1st order characterization method is standard and currently applied in geothermal boreholes (e.g. Häring et al.[1], Valley and Evans[10], Mastin et al.[11], Borm et al.[12], Brudy and Zoback et al.[13], Fernández-Ibáñez et al.[3]). However, it is very sensitive to the failure criterion used to compute borehole failure. Different failure criteria lead to different estimates of S_{Hmax} magnitude, depending on whether or not the effect of the intermediate principal stress, σ_2, is considered. Moreover, the rock strength properties defining the subjectively chosen failure criterion are hard to estimate from available borehole data. The choice of an appropriate failure criterion remains controversial. For example, Valley and Evans[10] used results from a single triaxial test on a core plug to parameterize their failure models and acknowledged the inherent and high uncertainties. Another approach consists of estimating rock strength properties by means of empirical relationships between strength and petrophysical parameters derived from sonic and density logs[14]. Such empirical relationships can be constrained by laboratory measurements on cores. Unfortunately, laboratory tests are time-consuming, expensive (and therefore often disregarded or, at best, carried out at one given depth) and rarely representative of in-situ conditions. Furthermore, It is also difficult to account for effects like core damage[15] that may hinder the estimation of strength properties.

State-of-the-art methods estimate stresses and strength properties separately relying heavily on very uncertain strength estimates. This work is aimed at filling this gap. We propose a systematic methodology to estimate depth profiles of the characteristics of the local stress tensor (both magnitudes and orientations of all three principal stresses) and rock strength properties (cohesion and friction) together. Both trends (1st order approximation) and/or variations around the trend (2nd order) can be estimated for each unknown. Model parameters are estimated via the regularized pilot points method[16,17] as implemented in PEST (Parameter ESTimation, Doherty[18]) from borehole cross-sectional characteristics (breakout width, breakout extent/depth of penetration and breakout orientation at different depths) and from the presence/absence of DITFs (including both axial and en-echelon drilling induced tensile fractures, referred to as A-DITFs and E-DITFs, respectively[13]) using the Kirsch analytical solution[19] to estimate the stress state around the borehole and appropriate failure parameter estimation approaches. All stress components around the borehole, including the remnant thermal stresses arising from the cooling of the borehole wall are accounted for. The inherent uncertainty on the choice of a failure criterion is taken into account through a sensitivity analysis, whose results allow to validate or discard failure models. For illustration purposes, the suggested methodology is applied to assess the variability of stress and strength along the 2.5 km crystalline section of the borehole BS-1 in Basel (Switzerland, Häring et al.[1]).

2. Methodology

The methodology suggested here is based on the five blocks sketched in Fig. 1, which are carried out in an iterative manner and at each borehole cross-section. The main steps of the algorithm are described in detail in the following subsections and itemized next:
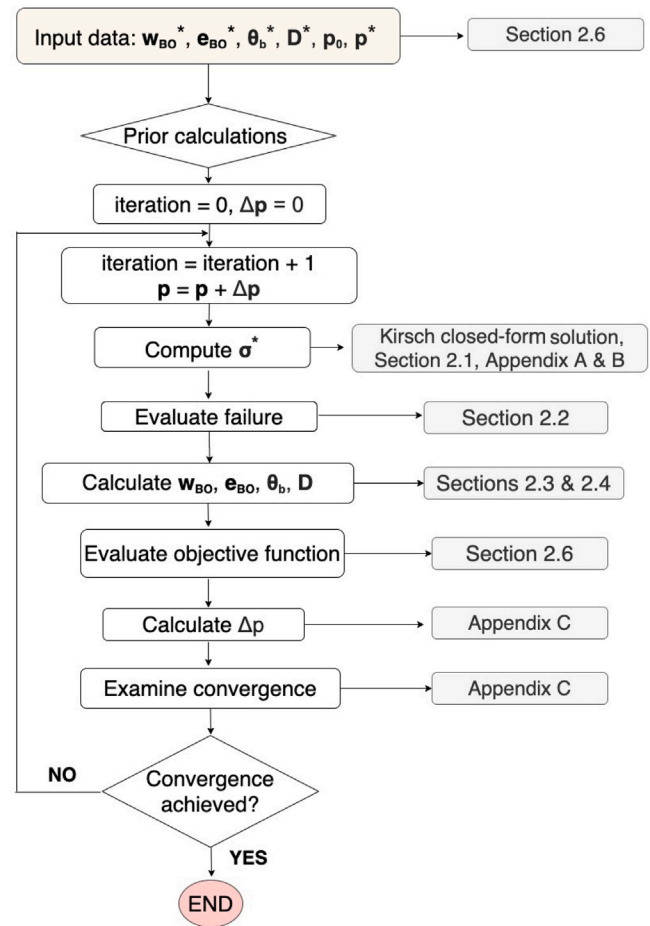

Fig. 1. Schematic description of the proposed methodology. In the insets, p_0 and $\boldsymbol{p}$ are the initial and sequentially updated sets of parameters, respectively; $\boldsymbol{w}$, $\boldsymbol{e}$ and $\boldsymbol{\theta}$ are vectors containing calculated breakout width, extent/depth of penetration and orientation; vector $\boldsymbol{D}$ represents the presence or absence of DITFs; the corresponding magnitudes with asterisk represent the measured counterparts.

- Step 1: given a set of initial parameters (e.g. depth trends of magnitudes, stress orientation, wellbore orientation, Poisson's ratio, thermo-elastic parameters, etc.), calculate stresses around the borehole using Kirsch analytical solution[19].
- Step 2: evaluate failure conditions. So far, Mohr–Coulomb and Mogi–Coulomb criteria have been implemented. Nonetheless, any other failure criterion can be implemented without loss of generality.
- Step 3: evaluate breakout width, extent and orientation, and the presence of DITFs.
- Step 4: evaluate an objective function (i.e., a penalty function) measuring the departure of the obtained solution from available measurements. Measurements include geometric features (i.e., borehole shape and presence/absence of DITFs), prior estimates of estimated parameters (e.g., a linear depth trend of a given parameter) or direct parameter measurements (e.g., of S_{hmin} after the interpretation of XLOTs).
- Step 5: modify parameters and go back to Step 1, until a minimum of the objective function is attained. This step is the so-called parameter estimation, optimization or, in broad sense, inverse problem[20]. The aforementioned workflow is carried out by the generic parameter estimation software PEST[18,21].

2.1. Calculation of the near-field state of stress

The stress redistribution caused by drilling and thermal effects can be calculated analytically or numerically. Analytical solutions are often preferred to complex numerical borehole models because they are (1) well established as standard practice in borehole design, (2) computationally faster, and (3) relatively simple to implement. The methodology presented here aims at obtaining fast and reliable near real-time calculations, which aids on-site decision-makings based on previously collected data (e.g., the direction and inclination of the deviated section of a borehole from data collected along the vertical initial section). In this work, we have chosen an elastic analytical solution[19,22] to compute the stress redistribution around the borehole. Our implementation of the Kirsch closed-form solution takes into account situations where the borehole is not aligned with one of the principal stresses. It further includes a thermo-elastic stress component to simulate the remnant stresses arising from the cooling of the borehole wall during drilling. The stress distribution is computed in two main steps, presented in detail in Appendices A and B of the supplementary materials. First, the stress tensor is expressed in a local and orthonormal borehole Cartesian coordinate system (u, v, w). Next, Kirsch equations are solved to compute the stress redistribution around the borehole in a cylindrical coordinate system with its origin at the centre of the borehole, (r, θ, w; r: radial, θ: tangential, w: axial).

The thermal stress components, $S_r^{\Delta T}$, $S_\theta^{\Delta T}$ and $S_w^{\Delta T}$ arising from any deviation from ambient temperature, ΔT, at the borehole wall are[23]:

$$S_r^{\Delta T} = 0 \tag{1}$$

$$S_\theta^{\Delta T} = S_w^{\Delta T} = \frac{\beta E \Delta T}{1 - \nu} \tag{2}$$

where E is the Young modulus, β is the coefficient of linear expansion and ν is the Poisson ratio. $\Delta T \geq 0$ denotes a temperature gain inside the borehole. These stress components are added to the corresponding components arising solely from the stress redistribution in response to excavation of the borehole Appendix (B).

Failure is computed from effective stresses, which are calculated from total stresses and pore pressure, P_p[24]:

$$\boldsymbol{\sigma} = \boldsymbol{S} - \gamma \delta_{ij} P_p \tag{3}$$

where P_p is fluid pressure, $\boldsymbol{S}$ and $\boldsymbol{\sigma}$ are the total and effective stress tensors, respectively, $\gamma \in [0\ 1]$ is the effective stress law coefficient[25–27] and δ_{ij} is the Kronecker δ which applies Terzaghi's correction to the normal components of $\boldsymbol{S}$ only. The effective stress law coefficient controls the degree of hydromechanical coupling[28] and its value is not excluded from debate because it depends not only on the type of rock, but also on rock microstructure[29]. In addition, it varies with time during failure[30]. Laboratory experiments evidence that Terzaghi's correction is valid for compressive failure even for low permeability rocks[31]. Recent experiments in the Grimsel Granite report Biot coefficients in the range 0.5 to 0.7[32]. In our work, we have chosen $\beta = 1.0$ because this value indicates the strongest possible hydromechanical coupling[28] regardless of the failure type (i.e., under compression or under tension).

The Kirsch closed-form solution is computationally attractive and is easy to implement. However, one must bear in mind the following assumptions and limitations:

1. It assumes CHILE material conditions (Continuous, Homogeneous, Isotropic and Linearly Elastic), which is generally not strictly true for rocks.
2. It assumes that the stresses are redistributed around a perfect cylinder. In other words, progressive failure is not considered.
3. It assumes an infinite cylindrical hole in a infinite medium. The stress rotations and magnitude changes associated with borehole drilling are neglected.

4. The scale effect is not taken into account as stresses at the borehole wall are independent of the borehole diameter.

These limitations can be tackled by means of numerical models or more complex closed-form solutions. For instance, transient failure can be modelled by analytical solutions including continuum plasticity with non-associated flow rules and strain softening[33] or continuum damage mechanics[34] or by hybrid continuum–discontinuum models[35–37]. Unfortunately, the aforementioned approaches are either hard to parameterize using standard data sets, involve a larger number of unknown parameter and are computationally intensive, which precludes parameter estimation (See Section 2.6).

2.2. Strength models

A main issue in the analysis of wellbore stability is the selection of an appropriate rock failure criterion. Without loss of generality, we focus here on two criteria: (1) the Mohr–Coulomb criterion[38,39], because it is the most used in practice and (2) the Mogi–Coulomb[40,41], which takes into account all principal stresses and has been shown to capture accurately true triaxial strength data.

The Mohr–Coulomb criterion assumes that σ_2 has no influence on rock strength, and is expressed in terms of principal stresses as:

$$\sigma_1 \geq C_o + q\sigma_3 \tag{4}$$

where C_o is the uniaxial compressive strength of the rock, and q is a material constant. Both C_o and q can be related to the internal friction angle, ψ, and the cohesion, c through:

$$q = \tan\left(\frac{\pi}{4} + \frac{\psi}{2}\right)^2 \tag{5}$$

$$C_o = \frac{2c\cos\psi}{1 - \sin\psi} \tag{6}$$

This failure criterion is standard in rock mechanics and its parameters are typically determined from conventional triaxial tests ($\sigma_1 > \sigma_2 = \sigma_3$). However, in practice, the Mohr–Coulomb criterion has been reported to be very conservative in predicting wellbore instability since it ignores the impact of σ_2. In fact, it was recommended[42,43] to use alternative failure criteria accounting for the influence of σ_2 on rock strength, such as the Mogi–Coulomb criterion to represent rock conditions more realistically. The latter relates the octahedral shear stress, τ_{oct}, to the mean stress, $\sigma_{m,2}$ as follows[41]:

$$\tau_{oct} \geq m + p \cdot \sigma_{m,2} \tag{7}$$

where:

$$\tau_{oct} = \frac{1}{3}\sqrt{(\sigma_1 - \sigma_2)^2 + (\sigma_1 - \sigma_3)^2 + (\sigma_2 - \sigma_3)^2} \tag{8}$$

and:

$$\sigma_{m,2} = \frac{(\sigma_1 + \sigma_3)}{2} \tag{9}$$

The parameters m and p are material constants that are also related to the internal friction, ψ and cohesion, c, by:

$$m = \frac{2\sqrt{2}}{3}c\cos\psi \tag{10}$$

$$p = \frac{2\sqrt{2}}{3}\sin\psi \tag{11}$$

Regardless of their formulation, failure criteria are difficult to parameterize. Both friction and cohesion can be measured in the laboratory. Unfortunately, this is rarely the case in practice because (1) retrieving cores from deep boreholes is expensive and time-consuming, and (2) laboratory conditions rarely represent in-situ conditions due to scale effects. A possible simplification is to set the cohesion to zero because that represents the worst case scenario (i.e., closest to failure). However, the cohesion of crystalline rocks can be large (e.g. in Basel,

cohesion ranges from 18.2 MPa to 35.5 MPa Valley and Evans[10]). To make things worse, uncertainties become critical in what concerns friction. Typically, the friction coefficient is set to 0.6, value qualified as that of the critically stressed crust[6,44]. Such value has been criticized by many authors on the basis of experimental data. For instance, laboratory analysis in the context of the Pohang EGS report values ~1.7[45] for an intact granite. Instead, Alcolea et al.[4] report low values in the range 0.4–0.45 for a fault zone in the same crystalline formation. Such relatively low values are not uncommon in faults[46–49], especially if they have suffered from weakening after seismic or aseismic slip episodes[50]. We consider the uncertainties inherent to strength parameters by means of model calibration (See Section 2.6).

2.3. Estimation of breakout width

The computation of breakout width, w_{BO}, consists of evaluating the failure criteria (Eq. (4) or (7)) at the borehole wall (i.e. $r = a$, $\forall\ \theta$) using the stresses calculated by the Kirsch closed-form solution. The arc, measured as angle, along which the failure criterion is met provides an estimate of w_{BO}. The assumption behind such computation is that failure occurs at the cylindrical borehole wall spanning an initial maximum width and then the breakouts progressively extend (deepen) but do not widen. Thus, it is not necessary to simulate the progressive failure leading to the final breakout geometry. Although some modifications of breakout width with time have been reported in-situ[51], the approach implemented in our methodology is widely accepted[5].

It is worth noting that breakouts with initially small size deepen as they grow, but do not further widen[6]. Consequently, stable wells can still be drilled that tolerate a degree of wellbore failure. Instead, initially wide breakouts can lead to washouts caused by the lack of intact material around the wellbore wall to withstand the applied stresses. In this work, it is important to highlight that the suggested method estimates model parameters from measurements available during or shortly after drilling, i.e., breakout width, breakout extent/depth of penetration, breakout orientation and drilling induced tensile fractures.

2.4. Estimation of breakout extent

Approaches to compute breakout extent, e_{BO}, are scarce in the literature. This is partly due to the fact that breakout width has been commonly preferred to estimate the stress state. Breakout extent is the result of progressive failure successively shedding the stresses and pushing failure deeper until a stable section is reached[52]. Such processes are difficult to simulate and, as a by-product, breakout extent has been disregarded. However, we argue that the characterization of breakout extent is crucial towards proper well completion, e.g., to guarantee effective packer sealing. In the following, we investigate computationally feasible alternatives to carry out this characterization.

Unfortunately, the application of the same general principle as for the computation of breakout width, i.e., evaluating the failure criteria for $r \geq a$ using the Kirsch solution is not meaningful because progressive failure is neglected.

An empirical criterion has been developed for brittle failure at tunnels[53] and applied to borehole failure[54]:

$$\frac{e_{BO}}{a} = 0.49 + 1.25 \frac{\sigma_{\theta\theta}^{max}}{C_o} \pm 0.1 \tag{12}$$

This criterion assumes (1) that the breakout extension, normalized by the nominal borehole radius, $\frac{e_{BO}}{a}$, is a linear function of the ratio of the maximum effective hoop stress, $\sigma_{\theta\theta}^{max}$, to the uniaxial compressive strength, C_o and that the wall strength is about half the uniaxial compressive strength. The wall strength can be estimated by the crack initiation level, which is typically about half the uniaxial compressive strength[55,56]. This relationship was developed using numerous field observations of enlargement of tunnel sections. Thus, its applicability

to breakout in boreholes, with a radius of curvature of the open space much smaller than in the tunnel cases on which this empirical criterion has been developed, is not yet established. Valley[57] analysing data from the well characterized deep geothermal project of Soultz-sous-Forêts, concluded that Eq. (12) tends to largely overestimate breakout extent in boreholes. This approach has been tested at early stages of this work without generating acceptable results. Thus, it is no longer considered in this manuscript for the sake of conciseness.

An alternative empirical approach is proposed by Shen[58]. The relationship was established upon numerical simulation of borehole failure using the fracture mechanics code FRACOD[59]. Shen's approach assumes a vertical borehole under plain strain conditions (FRACOD is a 2-dimensional code), i.e., one principal stress is aligned with the borehole axis, and dry conditions (no pore pressure, no borehole internal pressure) and he derived the following relationships between stress conditions, strength parameters and breakout extent:

$$\frac{3\sigma_{Hmax} - \sigma_{hmin}}{C_o} = 1 + A\left(\frac{e_{BO}}{a} - 1\right)^B \tag{13}$$

where $\frac{3\sigma_{Hmax}-\sigma_{hmin}}{C_o}$ represents the ratio of the maximum effective tangent stress to the uniaxial compressive strength. Under the constrains of Shen's relationship, the Kirsch solution simplifies and the maximum effective hoop stress becomes $\sigma_{\theta\theta}^{max} = 3\sigma_{Hmax} - \sigma_{hmin}$, σ_{Hmax} and σ_{hmin} being the maximum and the minimum effective principal horizontal stresses, respectively. A and B are regression parameters in the range[58]:

- Upper limit curve: $A = 21.2$, $B = 3.33$.
- Average curve: $A = 15.2$, $B = 2.67$.
- Lower limit curve: $A = 12.6$, $B = 2.22$.

In spite of its non-linearity, Shen's approach is computationally affordable. However, the strength is defined as a Rankine criterion, i.e. the minimum and intermediate principal stresses are ignored, which neglects the important stabilizing effect of the internal wellbore pressure (mud pressure). In our analyses, we extend Shen's criterion by defining an apparent wellbore strength σ_{app}, which accounts for the strengthening effect of σ_2 and σ_3, regardless of the chosen failure criterion. σ_{app} is evaluated at the borehole wall ($r = a$) and at an angle θ corresponding to the breakout centre, as calculated by the Kirsch closed-form solution. For the Mohr–Coulomb failure criterion, the apparent strength depends on the minimum principal effective stress, σ_3:

$$\sigma_{app} = q \cdot \sigma_3 + C_o \tag{14}$$

For the Mogi–Coulomb criterion, the apparent strength depends on both intermediate σ_2 and minimum σ_3 effective principal stresses (Eq. (7) to (9)). Resolving the maximum effective principal, σ_1, yields the estimate of the apparent strength σ_{app}:

$$\sigma_{app} = \frac{-(4\sigma_2 + 4\sigma_3 + 18mp + 9p^2\sigma_3)}{9p^2 - 8}$$
$$+ \frac{2\sqrt{6}\sqrt{12m^2 + 6mp\sigma_2 + 18\ mp\sigma_3 + 3p^2\sigma_2^2 + 9p^2\sigma_3^2 - 2\sigma_2^2 + 4\sigma_2\sigma_3 - 2\sigma_3^2}}{9p^2 - 8} \tag{15}$$

where m and p are the parameters of the Mogi–Coulomb failure criterion (Eqs. (10) and (11)).

Once the apparent strength has been determined, the depth of failure can be evaluated using the following modified Shen formula:

$$\frac{\sigma_1}{\sigma_{app}} = 1 + A\left(\frac{e_{BO}}{a} - 1\right)^B \tag{16}$$

where σ_1 is the maximum effective stress at the breakout centre point ($\theta = \theta_b$, see Appendices 3) computed with the Kirsch equations. A and B are fitting parameters, whose estimation is included in our methodology. It can be demonstrated that our modified relationship reduces exactly to that of Shen (Eq. (13)) when the internal wellbore pressure is ignored.

2.5. Estimation of DITFs occurrence

The occurrence of drilling induced tensile fracture is evaluated by the Rankine criterion:

$$\sigma_3 \le T_o \tag{17}$$

where T_o is the tensile strength (negative meaning tension). The minimum effective principal stress at the borehole wall, σ_3, is computed using the Kirsch solution presented in Appendices A and B and accounts for the wellbore internal pressure and the thermal stress arising from the cooling of the borehole wall. Note that both axial and en-echelon tensile fractures, A-DITFs and E-DITFs[13] are considered jointly in our implementation.

2.6. Parameter estimation

Our methodology, as any other stress characterization methodology, includes uncertain parameters (e.g., friction, cohesion, etc.). Commonly, parameter uncertainties are taken into account through parametric sensitivity analysis or by manual trial-and-error calibration at best. Instead, we cast the estimation problem in the mathematical framework of automatic inverse modelling, which frees the modeller of the burden of having to deal with complex, tedious, and prone to error testing of different parameter combinations. In broad terms, inverse modelling refers to the process of gathering information about the model from measurements of what is being modelled[20].

Once a conceptual model represented by equations (Sections 2.1 to 2.5 and Appendices A and B), the inverse problem, also known as history matching, tomography or calibration, consists of estimating the set (or sets) of parameters that best fit observations through the aforementioned mapping equations. This is achieved by minimizing a penalty function F, so-called objective function, which measures the misfit between calculated and observed values, arranged in vectors $\mathcal{O}$ and $\mathcal{O}^*$, respectively, with components $\mathcal{O}_i^* = \{w_{BO}^*, e_{BO}^*, \theta_b^*, D^*\}$. The set of calibrated parameters, described below, is arranged in vector $\mathcal{M}$. The objective function F can be expressed in a generic manner as:

$$F = \sum_{i=1}^{4} \lambda_i (\mathcal{O}_i - \mathcal{O}_i^*)^t V_i^{-1} (\mathcal{O}_i - \mathcal{O}_i^*)$$
$$+ \sum_{j=1}^{npar} \beta_j (\mathcal{M}_j - \mathcal{M}_j^*)^t V_j^{-1} (\mathcal{M}_j - \mathcal{M}_j^*) \tag{18}$$

where subscripts i and j stand for type of measurement ($i = 1$ for w_{BO}^*, $i = 2$ for e_{BO}^*, etc.) and parameter, up to $npar$ ($j = 1$ for parameters characterizing S_{Hmax}, $j = 2$ for those of S_{hmin}, etc.). The scalars λ_i and β_j are global calibration weights that balance the contribution of the individual pieces of information. Matrices V_i and V_j are the corresponding prior covariance matrices, which contain information about the initial uncertainty of each measurement/parameter type and the possible cross-correlations between them. Note that cross-correlation between measurements and parameters is not included in our calculations because these are already accounted for in the direct problem equations (e.g., in the Kirsch closed-form solution or in the expression of the chosen failure criterion). λ_i and β_j are global weights, whereas the inverse of matrices V_i and V_j can be viewed as a collection of individual, per-measurement, weights, δ. A more developed expression for the first term, of F, involving measurements only and assuming no correlation between measurements at different depths, can be written as:

$$F_m = \sum_{i=1}^{n} \lambda_{w_{BO,i}} \cdot \delta_{w_{BO,i}} \cdot (w_{BO,i} - w_{BO,i}^*)^2$$
$$+ \sum_{i=1}^{n} \lambda_{e_{BO,i}} \cdot \delta_{e_{BO,i}} \cdot (e_{BO,i} - e_{BO,i}^*)^2$$
$$+ \sum_{i=1}^{n} \lambda_{\theta_i} \cdot \delta_{\theta_i} \cdot (\theta_{b_i} - \theta_{b_i}^*)^2 + \sum_{i=1}^{n_{DITF}} \lambda_{D_i} \cdot \delta_{D_i} \cdot (D_i - D_i^*)^2 \tag{19}$$

where $\delta = \frac{1}{\sigma^2}$ is the inverse of the variance of each individual measurement (i.e., reporting on the degree of the confidence) and n_{DITF} is the number of DITFs observations. The second term, of parameters, in Eq. (18) can be developed similarly. Note that the formulation of F in Eqs. (18) and (19) is none other than that of generalized least squares of the well-known maximum likelihood method, which consists of maximizing the probability of observing the measured data with respect to the parameters (i.e., maximizing the parameters likelihood). Both allow to account for prior information of parameters[60]. As observed, the first term in F accounts for the misfit between calculated and observed breakout geometries and DITFs. The second, so-called plausibility term[17], penalizes the departure between parameter estimates and the corresponding prior information, arising, e.g., from prior studies, laboratory analyses and/or field tests like XLOTs. As such, we aim at finding not only the typically displayed "goodness of fit", but the goodness of fit achieved with reasonable, or plausible, parameter values. Note that w_{BO}^*, e_{BO}^* and θ_b^* are direct measurements. However, the presence/absence of DITFs is a binary variable (yes/no), which does not favour mathematical parameter estimation. To tackle this problem, we generate an estimate of the minimum hoop stress at the borehole wall consistent with observed DITFs. To that end, prior estimates of the mean tensile strength and of its standard deviation are required, which define a statistical Gaussian distribution of tensile strength, T_o. The raw observation is the total length of the borehole where DITFs are present standardized by borehole length, $L_D/L \cdot 100$ (%). With these data, a statistical distribution of the maximum hoop stress yielding DITFs at the corresponding measured depths is generated and arranged in vector D^*. The parameterization of the problem depends on the desired characterization. 1st order characterization aims at estimating depth trends. In such case, parameters are expressed in a generic manner as:

$$p = a \cdot TVD + b \tag{20}$$

Our methodology includes the segmentation of the borehole according to e.g., geological observations. Thus, parameters a and b can vary with depth in a step-wise manner, which allows us to consider, the presence of different strata yielding differentiated parameters depth profiles. Uncertain parameters, at each borehole segment, are the slope, a, and the shift, b, of all parameters intervening in the direct problem equations (See Section 5.1, and Appendices A and B in the supplementary materials). If segmentation is applied, calibrating different shifts may lead to discontinuous parameter profiles caused by, e.g., abrupt changes in the petrology of the column or the presence of a prominent shear zone. If smooth parameter variations between segments are preferred, then only the shifts b at the shallowest segment should be calibrated to grant continuity.

2nd order characterization aims at estimating the deviations of a given parameter from its estimated mean (1st order characterization), which enables the analysis of variability at all scales. To that end, we used the regularized pilot points method (RPPM, Alcolea et al.[17]), originally devised by De Marsily[61], as implemented in the free parameter estimation software PEST[18]. The generic parameterization now becomes:

$$p = a \cdot TVD + b + \epsilon(MD) \tag{21}$$

where ϵ is the perturbation of a parameters around its trend and it depends on measured depth to account for deviated boreholes. Note that the parameter a multiplies TVD instead, because most geomechanical parameters are expressed as vertical depth gradients (e.g., principal stresses, Häring et al.[1]). Indeed, MD and TVD are related univocally through the borehole trajectory.

Pixel-based methods have been developed for the continuum spatial estimation of parameters[62–64]. These reduce to a particular case of our formulation in which the vertical discretization step tends to zero[65], which boosts the number of estimated parameters and precludes the targeted "near real-time" calibration. Instead, we estimate variability

at selected so-called pilot points. The complete depth profile of a parameter is obtained by means of interpolation techniques. In our study, we use ordinary kriging[66,67], which smooths parameter variations. To that end, a variogram is inferred from the corresponding estimates at pilot points (and possibly, measurements). Note that each parameter is defined by its own set of pilot points. Thus, finer or coarser characterizations can be obtained for different parameters, depending on the pilot point discretization. The total number of pilot points may be larger than the total number of observations. In that case, the solution may become unstable[68]. To overcome this issue, two techniques are jointly used, i.e., singular value decomposition (SVD; Doherty[16]) and Tikhonov regularization[69]. SVD reduces the number of parameters being estimated, while regularization adds stability to the inverse problem solution by incorporating prior information on parameters (second term in Eq. (18)).

A key question is the optimal location of pilot points. The density of pilot points should be larger in areas where a finer characterization is needed. Another, less pragmatic and subjective alternative consists of placing pilot points randomly[17,70]; or according to adjoint sensitivity to identify the most sensitive/informative sections of the data sets[71].

The vector $\mathcal{M}$, which includes first and/or second order coefficients (a and b, and ϵ at pilot points for all parameters) is updated by PEST in an iterative manner using the Levenberg–Marquardt algorithm[72]. PEST also allows to include upper and lower bounds to each estimated parameter. As observed, the parameterization for the 2nd order characterization includes that for the 1st order characterization, and all parameters (a and b, and ϵ at pilot points) can be estimated together. However, prior studies in the context of this work reveal that depth trends estimated in this manner do not deviate much from those estimated as raw 1st order method (i.e., a and b only). Thus, our calibration is made in two steps. First, depth trends of parameters are estimated. Second, 1st order parameter values at pilot point locations are used as prior information for the 2nd order characterization. For illustration purposes, the suggested methodology is applied to the data set of borehole BS-1 in Basel, described next.

It is worth noting that "characterization" and "estimation/calibration" have two different meanings. On the one hand, characterization refers to the conceptualization of the stress field and the underlying parameterization. On the other hand, calibration is the process of estimating the key parameters involved in the characterization. This vicious circle causes that, in the inverse problem literature, both terms are used indistinctly.

3. BS-1 data description

In 2006, a 5 km deep borehole, termed BS-1, was drilled to the crystalline basement in Basel (Switzerland) as part of a planned EGS doublet[1]. In the crystalline basement, from 2516 m MD, the wellbore diameter was 9–7/8" down to 4850 m MD. The borehole was then drilled to a total depth of 5009.4 m MD with a diameter of 8–1/2". The borehole is sub-vertical with a maximum deviation from the vertical of 8°. MD was measured from the rotary, located 9.14 m above ground level.

The crystalline basement was described on-site by observing cuttings[73], and only a 10 m long core was retrieved at a depth of 4909 m MD. The composition of the granitic basement rock is generally homogeneous with slight variations in quartz content from monzogranite to monzonite. Alteration associated with brittle shear zones is present locally along the borehole. Ziegler et al.[74] obtained an average fracture frequency that decreases with depth (3.1, 1.3 and 0.3 fractures/m at depth ranges 2.6–2.65 km, 2.65–3.0 km, and below 3.0 km, respectively). The upper 400 m of the crystalline section of BS-1 are interpreted as influenced by paleo-exhumation during the Permo-Carboniferous prior the sedimentation of the Mesozoic and Cenozoic cover. Thus, this zone may be affected by a perturbed stress state, either

as a remanence of pre-sedimentation exhumation and relaxation or in response to more recent tectonic loadings.

Ultrasonic borehole televiewer (UBI) logs with azimuthal resolution of 2° were run between 2578 and 5001 m MD shortly after drilling[75]. The fluid velocity in the borehole was measured during the trip in hole and used to compute wellbore geometry from transit time data. The open hole crystalline section was subject to an extensive logging programme before setting a 7–5/8" casing with its shoe at a depth of 4638 m MD. A reservoir characterization phase was conducted in the open hole section below the 7–5/8" casing shoe. Finally, a hydraulic stimulation was performed in December 2006, which caused a felt 3.4 event magnitude and ultimately led to the abandonment of the project[1,76].

3.1. BS-1 failure data

The borehole data used in our analysis and the procedure to infer borehole failure are described in Valley and Evans[10,75]. Breakouts were identified along 81% of the logged section and are almost continuous except for a large gap from 2747 m TVD to 2899 m TVD and some other minor gaps at 3820–3856 m TVD, 4185–4221 m TVD and 4582–4631 m TVD (Fig. 2). The aforementioned borehole segments coincide with those of strong intensity of natural fractures. This paradox, involving the coalescent presence of natural fractures but the absence of borehole breakouts, occurs frequently in deep boreholes and is attributed to local stress heterogeneities and to the impact of thermal stresses as discussed in Section 6. Borehole geometry was averaged from the inferred breakouts at cross sections with a longitudinal spacing of 40 cm (5001 sections for each type of measurements, and, overall, 20004 sections; see an example in Fig. 3).

Table 1 summarizes the statistical description of borehole failure along BS-1. Breakouts are pervasive along BS-1 (81%), whereas DITFS are present along 20% of the borehole only. As already observed by Valley and Evans[10], breakout width, w_{BO} decreases with depth from an average of 94° in the 2.58–3 km section to 65° in the 4.5–5 km section (Fig. 2b). Normalized failure extension, $\frac{e_{BO}}{a}$, remains relatively constant with depth (only a slight increase with depth is observed). The change of diameter from 9–7/8" to 8–1/2" at 4850 m MD does not impact significantly breakout geometry. Considering all data, the average of θ_b is 54°[75]. The variability of breakout orientation is shown to follow scaling laws[77] and can differ significantly from the mean orientation at the local scale, which is typically attributed to the presence of natural fractures and other sources of local heterogeneity. Correspondingly, the standard deviation of breakout orientation is 14°[75].

Overall, 20% of the logged section was affected by DITFs (A-DITFs and E-DITFs, Fig. 2g). As observed, there are not obvious depth trends in the distribution of DITFs. This suggests that, along the entire borehole length, σ_3^{min} at the wellbore wall is not far from tensile failure and additional hoop stresses caused by cooling of the borehole wall are sufficient to induce locally tensile failure. This is further discussed in Section 6.

DITFs observations are transformed into minimum hoop stress (in vector $\mathbf{D}$, Eq. (19)). In the presence of DITFs, the minimum hoop stress must be lower than tensile strength ($T_o = -4$ MPa, tension being negative), whereas the minimum hoop stress remains higher than the tensile strength in the presence of DITFs. In greater detail, 20% of the BS-1 profile is affected by DITFs. We generate a minimum hoop stress distribution respecting the observations of DITFs occurrences. This allows converting the boolean DITFs observations (occurrence or absence) into a continuous variable which is better suited for our calibration algorithm.

3.2. BS-1 stress state from previous studies

Häring et al.[1] provided an initial assessment of the stress state. Valley and Evans[75] assessed the orientation of the maximum horizontal
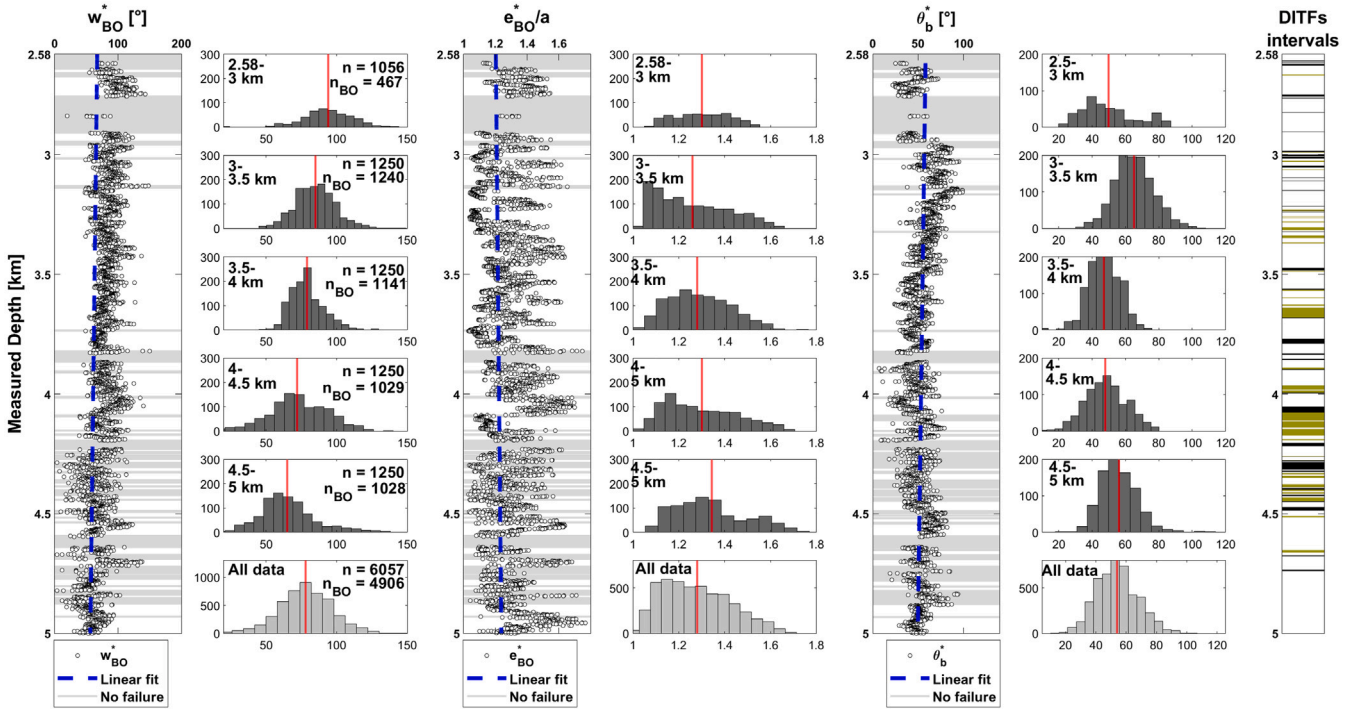
Fig. 2. Interpreted failure data along borehole BS-1: (a, c and e) Spatial distribution of breakout width (w_{BO}), extent normalized by borehole radius (e_{BO}/a) and orientation (θ_b), respectively. The dashed lines represent linear depth trends and the horizontal grey shaded zones represent cross-sections without breakouts; (b, d and f) histograms of the aforementioned magnitudes along 500 m long borehole sections and considered altogether (panels on bottom). The insets report on the number of sections (n) and the number of sections where breakouts occur (n_{BO}). The red lines depict mean values; (g) Observed DITFs intervals (green = en-echelon; black = axial). (For interpretation of the references to colour in this figure legend, the reader is referred to the web version of this article.)
Source: Modified from Valley and Evans[75].

Table 1
Statistical parameters of key breakout indicators.

Cross sections every 40 cm from 2.58 to 5 km MD:	$n = 6057$			
Sections with identified breakouts:	$n_{BO} = 4906$			
Percentage of wellbore length affected by breakouts:	81%			
	min	max	mean	std
w_{BO}:	15°	150°	78°	19°
$\frac{e_{BO}}{a}$:	1.03	1.81	1.28	0.15
θ_{BO}:	7°	170°	54°	14°
Sections with identified DITFs:	$n_{DITFs} = 1211$			
Percentage of wellbore length affected by DITFs :	20%			

stress. Valley and Evans[10] used breakout width data to estimate stress magnitudes. The analyses of microseismicity associated with the stimulation in BS-1[76,78–80] gave some further insights on the stress state. A detailed discussion of the stress magnitudes at the Basel Geothermal site is given in Valley and Evans[10] and we refer the interested reader to this publication for details out of the scope of this paper. We report here only on the so-called 1st order characterization, i.e. linear depth trend of the magnitude of S_v, S_{hmin}, S_{Hmax} and P_p and of the azimuth of S_{Hmax}. Fig. 4 summarizes the published profiles.

The main discrepancies between prior studies concern the S_{hmin} and S_{Hmax} profiles. The profiles proposed by Valley and Evans[10] share the commonality of a very low stress gradient that are required to explain the fact that breakout width decreases with depth and assuming that the borehole wall strength remains constant with depth, as supported by the homogeneity of the rock along the BS-1 basement section. The absolute value of S_{Hmax} is highly uncertain because it depends strongly on the chosen failure criterion and its parameterization, for which there are no robust evidences. The focal mechanism of induced seismic events indicate a mix of strike-slip and normal faulting regimes at the level

of the reservoir. The stress profiles proposed by Valley and Evans[10] are consistent with this observation. All proposed profiles are also consistent with the limits imposed by frictional strength of the earth crust.[5]

4. Parametric and sensitivity analyses

In this section, we summarize a series of parametric and sensitivity analyses carried out prior to parameter calibration, aimed at understanding the influence of each parameter intervening in the formulation of the stress and failure models. Identifying the critical parameters will help us to (1) reduce the parameterization, and (2) bound the parameter space. Furthermore, we illustrate the problem of non-uniqueness by calibrating parameters at the cross-section MD = 3509 m in Fig. 3.

4.1. Relationship between breakout width and breakout extent in the BS-1 well

Fig. 5 displays the cross plot of measurements of breakout width and extent along the BS-1 well. The data present the expected positive
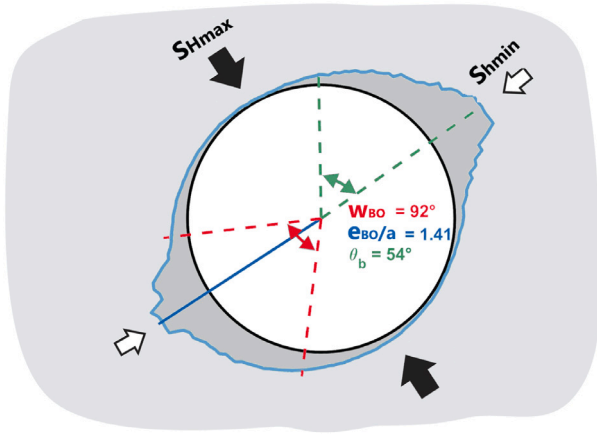
Fig. 3. Geometry of the BS-1 borehole at 3509 m MD. The black circle corresponds to the normal bit size (a = 9–7/8") and the blue envelop corresponds to the inferred geometry of the BS-1 borehole. A breakout width w_{BO} = 92°, a normalized breakout extent $\frac{e_{BO}}{a}$ = 1.41 and a breakout orientation θ_b = 54° were measured. (For interpretation of the references to colour in this figure legend, the reader is referred to the web version of this article.)

correlation, i.e., as borehole failure severity increases, both breakout width and extent increase. However, and in spite of data scattering, some underlying non-linear trends can be identified. For instance, wide breakouts with limited extent are observed along the shallower section of the borehole (blueish dots in Fig. 5). Instead, breakouts are relatively narrower at greater depth (yellowish dots) for a similar extent. In order to identify what parameters control such trends, we explore first in a generic manner the conditions controlling the relative width and extent of breakouts.

An obvious condition influencing the relationship between width and extent of breakout is the difference between stresses in the plane normal to the borehole. To illustrate this effect, we consider the simple case of a vertical borehole in a stress field with one principal stress being vertical. The effect of the differential horizontal stress, $\Delta\sigma_h = \sigma_{Hmax} - \sigma_{hmin}$, is illustrated in Fig. 6a–b using arbitrary numerical values

to facilitate comprehension and the reproducibility of our numerical experiment. In Fig. 6a, we present a case with $\Delta\sigma_h$ = 2 MPa. The variation of the maximum principal stress at the borehole wall is 8 MPa (from 94 to 102 MPa). Assuming a borehole wall strength C_o = 100 MPa, the resulting breakout width is 60° and the normalized breakout extent is 1.08 (corresponding to a maximum stress at the borehole wall of 102 MPa, 2 MPa above C_o; see Sections 2.3 and 2.4). Fig. 6b explores the same conditions using a highly anisotropic stress tensor with $\Delta\sigma_h$ = 20 MPa. In this case, the variation of the maximum principal stress at the borehole wall is much larger ($4\Delta\sigma_h$ = 80 MPa). We deliberately choose absolute value of the stress magnitude leading to the same breakout width of 60°. In this case, the normalized breakout extent is 1.2 (corresponding to a maximum stress at the borehole wall of 120 MPa, 20 MPa above C_o). We conclude from these two examples that (1) for larger $\Delta\sigma_h$, breakouts with identical width will have a larger extent, and (2) in broad terms, small $\Delta\sigma_h$ tend to generate wide and shallow breakouts whereas large $\Delta\sigma_h$ will tend to generate narrow and extended breakouts. Note that, for simplicity, we have chosen a simple situation in which the hoop stress is always the maximum principal stress and a failure criterion independent of the intermediate stress. Indeed, this is not always the case in practice, and more complex conditions would lead to less obvious computations of breakout width and extent according to the equations in Section 2, which are generic.

Another key point is the asymptotic behaviour of the equations governing breakout width[57], manifested in the so-called pivot points depicted as black triangles in Fig. 6c–d. The stress curves displayed in Fig. 6c–d are built by setting and increasing incrementally σ_{Hmax}. All the curves share a common pivot point corresponding to an angular opening of 120°. The stress magnitude at the pivot point is equal to $2\sigma_{hmin}$ (Eq. (B.3)) for isotropic stress conditions. When the pivot point is close to the failure line (Fig. 6c, $2\sigma_{hmin}$ = 96 MPa), breakouts tend to be shallow. On the contrary, when the pivot point is far from the failure line (Fig. 6d, $2\sigma_{hmin}$ = 76 MPa), extended breakouts are generated. As a direct comparison, the lower line in Fig. 6c and the upper line in Fig. 6d yield the same breakout width of 60°, relative breakout extent of 1.08 and 1.16 respectively. Thus, the ratio $\frac{\sigma_{hmin}}{C_o}$ has a strong impact on the relationship between breakout width and extension. When pivot
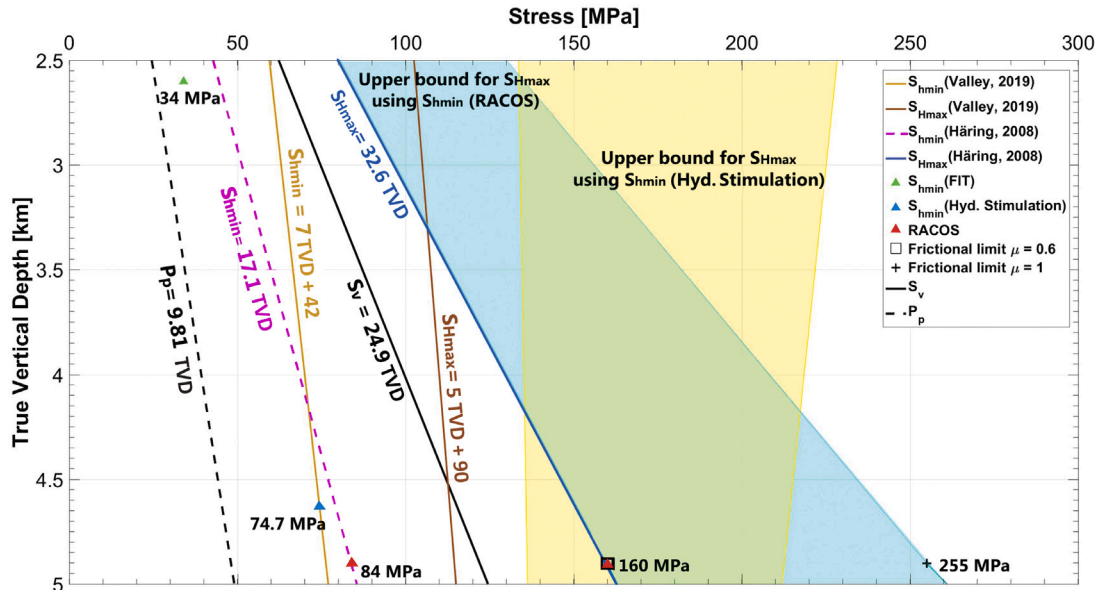

Fig. 4. Constraints on S_{hmin} and S_{Hmax} in the BS-1 well inferred from hydraulic data, FIT test and RACOS[81] as compiled by Häring et al.[1] Profiles of S_{Hmax} and S_{hmin} from Valley and Evans[10] are also presented. The coloured areas depict upper bounds for S_{Hmax} considering frictional equilibrium[6], friction coefficients between 0.6 and 1.0 and the two proposed profiles of S_{hmin}. The orientation of S_{Hmax} is common to all analyses, i.e., $144 \pm 14°$[75]. (For interpretation of the references to colour in this figure legend, the reader is referred to the web version of this article.)
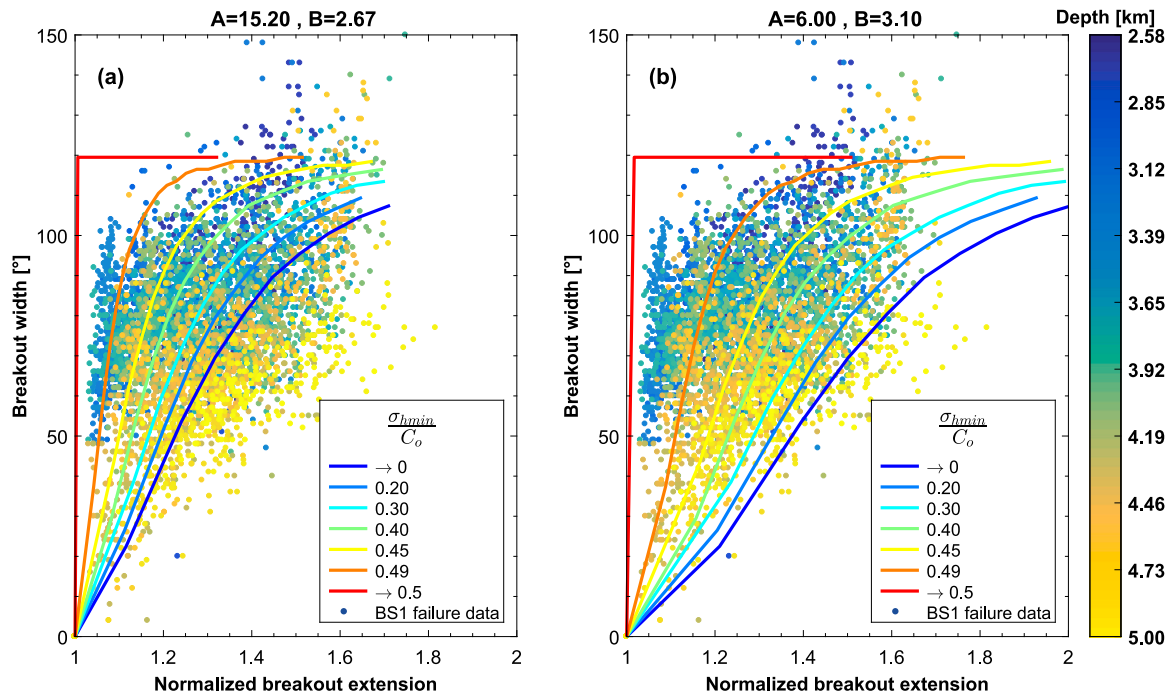
Fig. 5. BS-1 borehole failure data and failure models. Dots represent measurements and are coloured according to TVD. Failure models are depicted for different values of the ratio σ_{hmin}/C_o[58] and different values of the governing parameters: (a) mean values suggested by Shen[58]; (b) modified values after a preliminary calibration exercise. (For interpretation of the references to colour in this figure legend, the reader is referred to the web version of this article.)

points are located exactly at the failure line, i.e., when $\frac{\sigma_{hmin}}{C_o} = 0.5$, the breakout width is always 120°.

Failure models corresponding to different values of $\frac{\sigma_{hmin}}{C_o}$ are superimposed to the Basel breakout width-extent data set in Fig. 5. In broad terms, the suggested failure model explains well the dispersion of data observed along BS-1. Note that, in our failure model, the relationship between breakout width and extent is controlled by the parameters A and B in Eq. (13). The lines in Fig. 5a display the failure criterion using the average parameters suggested by Shen[58] i.e., $A = 15.2$ and $B = 2.67$. As observed, the envelope of solutions obtained in the maximum possible ranges of $\frac{\sigma_{hmin}}{C_o} \in [0, 0.5]$ does not fully cover the breakout geometries at greatest depths (TVD > 4000 m). Fig. 5b displays the same setup, but now using $A = 6$ and $B = 3.1$, attained after a preliminary calibration exercise. The coverage of breakout geometries is now better regardless of depth, as expected. We attribute this to the fact that Shen's parameters depend on rock type (and heterogeneity) and, therefore, must be calibrated.

4.2. Sensitivity analyses

Sensitivity analyses are useful to identify parameters with large impact on model outputs, i.e., those to be calibrated, and to bracket parameter ranges, thus reducing prior uncertainties and computational effort. We use as base case the breakout at 3509 m MD displayed in Fig. 3, which we consider as representative of the entire borehole length. A set of base case parameters (Fig. 7) is defined that leads to a good fit of either breakout width or breakout normalized extent. Note that different rock strength parameters are used in both cases, which allows us to identify the parameters controlling breakout geometric features separately. Incremental parametric variations of 1% are applied to each parameter in a range ± 20% of the base value, while the remaining parameters are set to the base case value. The solution, either w_{BO} or e_{BO} is computed and represented as "tornado plots" in Fig. 7. Note that the shape of each bar is the result of an individual sensitivity analysis. A linear relationship between a parameter and

an output (breakout width/extent) is seen as a perfect triangular bar (e.g., P_m). Instead, nonlinear relationships are seen as "thorny" or "bulgy" bars (e.g., S_{Hmax} and S_{hmin}, respectively) reflecting the nature of the correlation.

We have limited the analysis to w_{BO} and e_{BO} because breakout orientation is directly inferred from breakout geometry (and is therefore not parameterized) and the presence/absence of DITFs depends only on stresses and the cooling. As expected, the most influencing parameter in both cases is the internal well pressure, P_m. The second most influencing parameter is S_{Hmax}. Moreover, S_{hmin} plays generally a very important role and must necessarily be calibrated. The apparent wall strength plays also an important role on breakout geometry. As such, it is not strange that model outputs are overly sensitive to both cohesion and friction (in fact, to a suitable combination of them). Last, Shen parameters A and B also play an important role in the final breakout extent. To make the long story short, the chosen parameterization for the calibration in Section 5 is as follows:

- It is assumed that the vertical stress, S_v, is principal and known, which greatly reduces the number of model parameters. This is justified by the observed small deviations of the density log around its linear depth trend and is attributed by the homogeneity of the crystalline section of the BS-1 borehole observed in the cuttings retrieved during drilling.
- In the same line of arguments, the azimuth of the maximum principal stress S_{Hmax} and the strength parameters (internal friction angle, ψ, cohesion c, and modified Shen's parameters A and B) are considered constant in the 1st order approach. Nonetheless, our methodology is generic and linear depth trends can be accommodated for any of the aforementioned parameters. The parameters controlling thermal stresses, E and v, are assumed constant and known. In fact, they are usually inferred after the dynamic to static correction of the sonic log in the best case or inherited from existing literature in most cases. The impact of stiffness variations is discussed in Section 6.
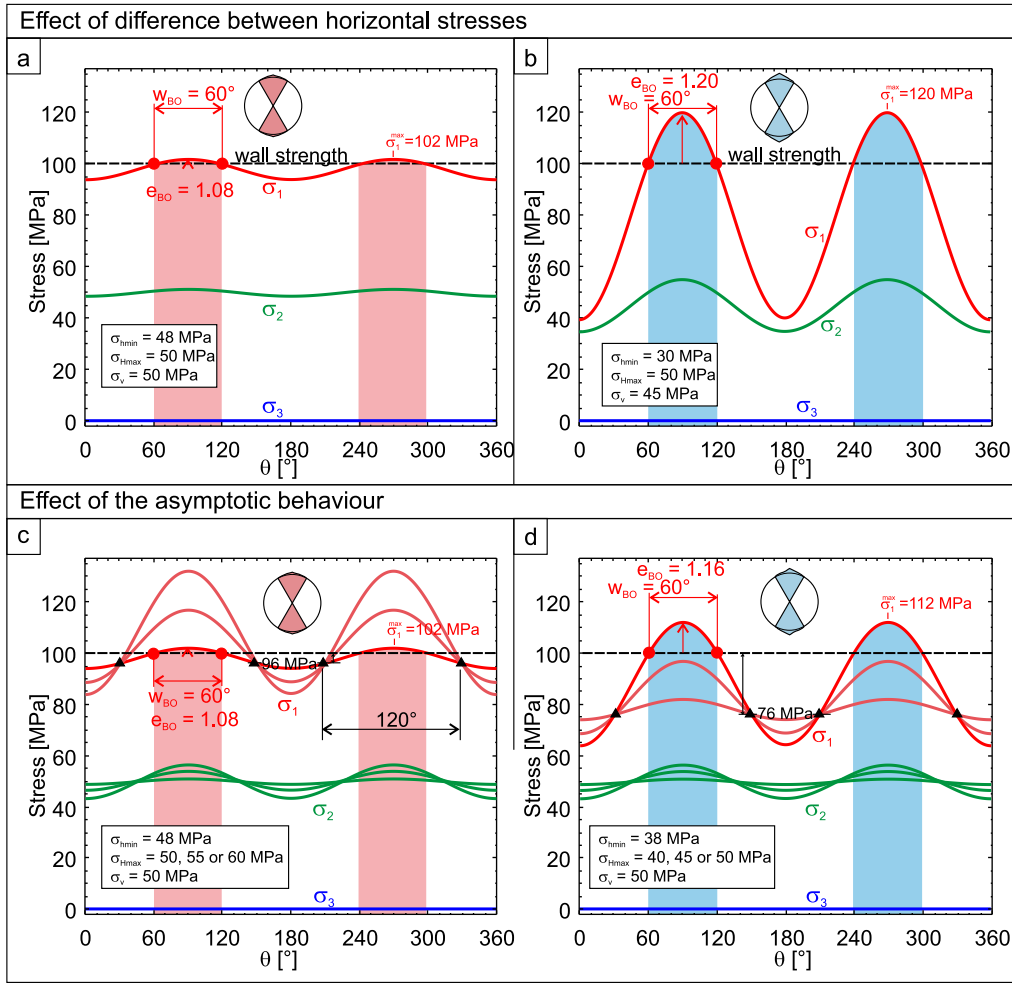
Fig. 6. Illustration of the effect of stress conditions controlling the relationship between breakout width and extension. The principal stresses (σ_1, σ_2 and σ_3) at the wall of a vertical borehole are shown in red, green and blue, respectively, for conditions generating 60° breakout width but a variable breakout extent. In all cases, a vertical borehole is considered with far field stress σ_v aligned with the borehole axis and σ_{Hmax} and σ_{hmin} normal to it. Borehole internal fluid pressure, P_w, is taken as 0 MPa and borehole wall strength, C_o, as 100 MPa. (a) Example with similar horizontal stresses ($\Delta\sigma_h = 2$ MPa) leading to shallow breakouts. (b) Example with dissimilar horizontal stresses ($\Delta\sigma_h = 20$ MPa) leading to extended breakout. (c) Example with the pivot point close to the borehole wall strength leading to shallow breakouts. (d) Example with the pivot point low compared to the borehole wall strength leading to extended breakouts. (For interpretation of the references to colour in this figure legend, the reader is referred to the web version of this article.)

- In the absence of further information, the distribution of formation pressure is assumed to be hydrostatic, which further reduces the parameterization. Although for example at the BS1 site, a slightly artesian conditions are encountered, we argue that deviations from the hydrostatic distribution are small compared to uncertainties on other model parameters.

The chosen first order parameterization, summarized in vector $\mathcal{M}$ is:

$$\mathcal{M} = \{a_{S_{Hmax}}, b_{S_{Hmax}}, a_{S_{hmin}}, b_{S_{hmin}}, \alpha, c, \psi, A, B\} \qquad (22)$$

The parameter α in this first order parameterization refers to Euler's angle (see Appendix A). The second order characterization is carried out by estimating optimum parameters values at a set of pilot points (common to all parameter type, and is discussed in detail in Section 5.1.1).

4.3. Illustration of solution non-uniqueness

Inverse problem often suffers from instability, non-identifiability and non-uniqueness. Carrera and Neuman[82] discuss extensively these concepts and show that they are closely related. Instability is present when small changes in the observations lead to large changes in the estimated parameters, and is tackled by using model identification criteria[17,83–89]. Non-identifiability occurs when more than one set of parameters leads to a given solution of the forward problem. Non-uniqueness is present when more than one set of parameters leads to a minimum of the objective function F. We illustrate non-uniqueness by calibrating only S_{Hmax} and C_o at the cross-section in Fig. 3. All other parameters are set to the corresponding base case values. Furthermore, the impact of the parameters of the modified Shen's criterion is also evaluated by comparing the breakout extent attained with three different pairs of values (A, B). Results are summarized in Fig. 8, which shows combinations of C_o and S_{Hmax} reproducing the geometry of the breakout. The first obvious observation is that for any given C_o, a value of S_{Hmax} exists that reproduces exactly the observations and that the calibrated pairs of C_o and S_{Hmax} are almost linearly correlated. This is consistent with Barton's equation[90], developed for the estimation of S_{Hmax} based on breakout width observations. Unfortunately, C_o is usually unknown (or known at certain sections at best) and thus the problem is under-determined.

As expected, the calibrated pairs (S_{Hmax}, C_o) reproducing breakout width (red curve in Fig. 8) do not capture properly the breakout extent and vice versa. The only sets of parameters reproducing both geometric features are the intersections between the calibrated w_{BO}
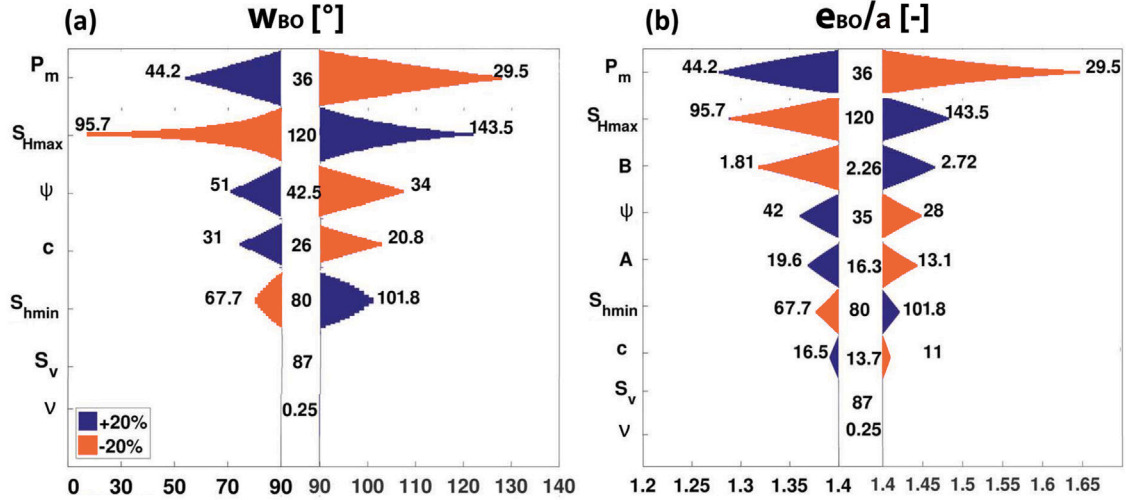
Fig. 7. Tornado diagram summarizing the sensitivity analyses: (a) breakout width [°]; (b) normalized breakout extent [–]. The analysed parameters are: mud pressure, P_m [MPa], maximum and minimum principal horizontal stresses, S_{Hmax} and S_{hmin}, respectively [MPa], principal vertical stress, S_v [MPa], internal friction angle, ψ [°], cohesion, c [MPa], Poisson ratio, v [–] and Shen's parameters, A [–] and B [–]. Base case values of analysed parameters are displayed at the centre of the tornado plot. Note that different values are used for the sensitivity analysis of width and extent. The minimum and maximum values of inputs (in the range ±20% with respect to the base values) are typed to the left and right of each diagram, respectively. Stress parameters are common to both cases ($S_v = 87$ MPa, $S_{Hmax} = 1.37 S_v$, $S_{hmin} = 0.97 S_v$). A common Poisson ratio $v = 0.25$ and Young modulus $E = 65$ GPa were used.
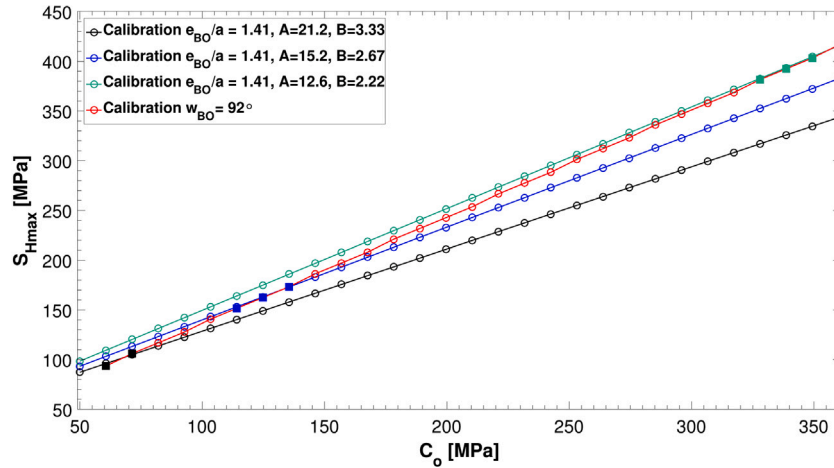

Fig. 8. Illustration of non-uniqueness after the calibration process at the cross-section at 3509 m MD. The curves depict the calibrated pairs (S_{Hmax}, C_o) capable of reproducing either a breakout width of 92° or a normalized breakout extent of 1.41. The latter is carried out using three different pairs of values of Shen's parameters A and B. The borehole is assumed to be vertical. The other parameters used for this basic calibration are: $S_{hmin} = 48.6$ MPa, $S_v = 87$ MPa, $P_p = 34.4$ MPa, $P_m = 1.07 \cdot P_p$, $\psi = 30°$, $v = 0.25$, $E = 65$ GPa. The filled squares represent the calibrated pairs (S_{Hmax}, C_o) for which we reproduce jointly w_{BO} and e_{BO} at 3509 m MD.

and $\frac{e_{BO}}{a}$ (squares in Fig. 8), which depends on the value of the Shen's empirical parameters A and B, not known a priori. Thus, considering simultaneously both breakout width and extension at a certain section does not allow to converge to a unique optimum parameter solution at a certain borehole cross-section. Fortunately, adding other sources of measurements (i.e., breakout orientation, DITFs and, especially, prior information on model parameters) helps to alleviate non-uniqueness[17,20].

5. Calibration of the developed geomechanical model on observed failure in the BS-1 well

In this section, we present the calibration results using measurements from 3 to 5 km MD. We first focus on the 1st order characterization, i.e., the estimation of linear trends of parameters with depth. We argue that 1st order characterization is necessary, but not sufficient to warrant proper completion (e.g., cementing or packer sealing). Thus,

we analyse the variability of model parameters by calibrating the deviations with respect to the trend at 201 pilot points, whose location is common to all parameters (i.e., overall 1407 pilot points). We call this stage 2nd order calibration.

5.1. First order calibration approach

To reproduce BS-1 observations with our failure models, we focus on the model parameters that are the most influential and cannot be estimated otherwise. In this 1st order calibration, we use simplified profile with depth of these model parameters (Eq. (20)). In summary our stress/strength model is parameterized by 9 parameters (Eq. (22)). A number of starting points is used in the calibration to guarantee that a global optimum is achieved by the Levenberg–Marquardt algorithm[91]. To that end, the prior distribution of each parameter is randomly sampled assuming a uniform distribution, which renders overall 200 initial parameterizations that explore the global parameter space. An
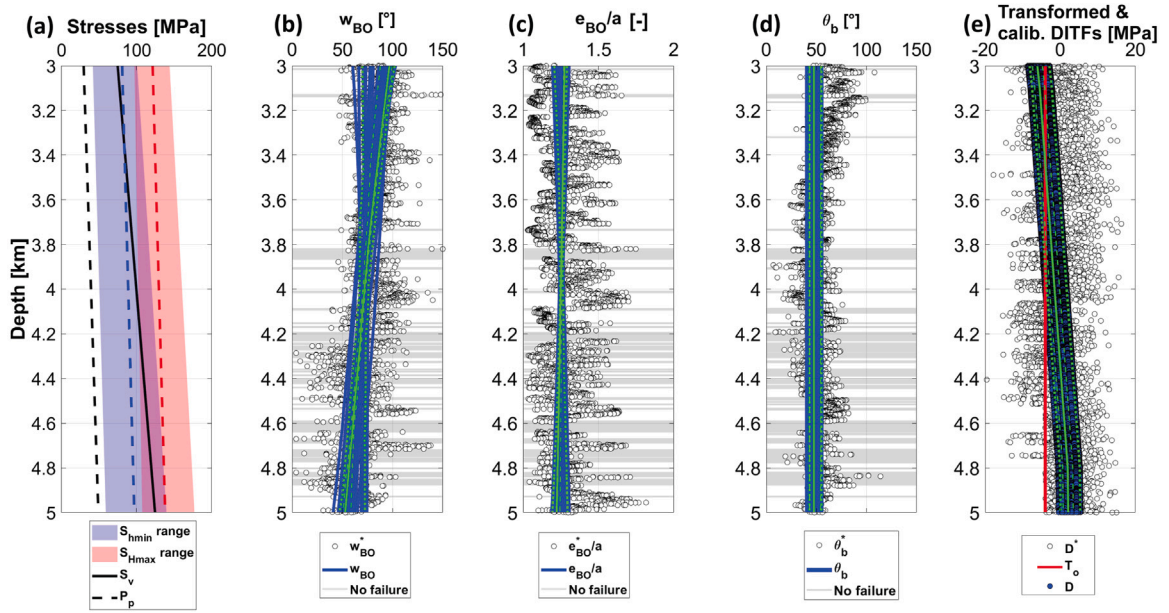
Fig. 9. 1st order calibration results using the Mohr–Coulomb failure criterion. (a) range of the calibrated S_{Hmax} (pink) and S_{hmin} (purple) for 136 different starting points. S_v and pore pressure profiles are depicted by the solid and dashed black lines, respectively. The blue and red dashed lines depict the mean of the ranges of the calibrated S_{hmin} and S_{Hmax}, respectively; (b) calibrated and measured breakout width; (c) normalized breakout extent; (d) breakout orientation; (e) DITFs. In panels (b) to (d), the black symbols depict measurements, whereas in panel (e), they depict the estimated minimum hoop stress derived from DITFs observations. In panels (b) to (e), the blue lines represent the outputs of the calibrated models. The grey shaded zones represent depth ranges without breakouts. The red line in panel (e) corresponds to tensile strength, $T_o = -4$ MPa. Finally, the solid green lines correspond to the mean of the outputs of the 136 accepted models, whereas the dashed lines represent the 25th–75th and 5th–95th percentiles. (For interpretation of the references to colour in this figure legend, the reader is referred to the web version of this article.)

initial rejection criterion, based on frictional equilibrium, is applied to the initial starting points, as follows:

1. Sample the parameter space.
2. Check coherency and frictional equilibrium[6,92]:

   - $S_{Hmax} \geq S_{hmin}$
   - $\dfrac{S_1 - P_p}{S_3 - P_p} \leq [\sqrt{\mu^2 + 1} + \mu]^2$

   where S_1 and S_3 are the maximum and the minimum total principal stresses respectively, P_p is the pore pressure and μ is the friction coefficient ($\mu = \tan(\psi)$).

Initial sets of parameters not meeting the aforementioned constraints are rejected and new ones are generated until the target 200 initial coherent parameterizations is achieved. Note that initial sets of parameters may lead to different final optimum sets of calibrated parameters with similar final value of the objective function F. This is a common issue in inverse problem theory, known as non-uniqueness, and is discussed in detail in Section 5.1.1.

Assumptions are required for model parameters that are not calibrated. We use the following equations for S_v and P_p:

$$S_v \text{ [MPa]} = 24.9 \cdot TVD \text{ [km]} \tag{23}$$

$$P_p \text{ [MPa]} = 9.81 \cdot TVD \text{ [km]} \tag{24}$$

Based on the mud density measurements collected during the drilling of BS-1, we assume a hydrostatic mud pressure corresponding to an equivalent mud density, $\rho_{mud} = 1.07$ g/cm^3. We use the actual BS-1 borehole trajectory in our computations. Different cooling profiles for breakouts and DITFs after Valley and Evans[10] were used to estimate thermal stresses as well as the Young modulus ($E = 65$ GPa) and the coefficient of linear expansion ($\beta = 10^{-5}$ K^{-1}). In addition, a set of bounding thresholds is implemented in PEST to minimize unwanted and large parameter oscillations.

5.1.1. Non-uniqueness

A posterior rejection criterion was defined by setting a maximum threshold for the objective function after calibration, and calibrated models with final objective function above the threshold were rejected. After this rejection process, only 136 and 95 well calibrated models were kept using the Mohr–Coulomb and Mogi–Coulomb failure criteria, respectively.

Fig. 9 shows failure observations (w_{BO}^*, $\frac{e_{BO}}{a}^*$, θ_b^* and D^*) and the 136 well calibrated horizontal principal stresses using the Mohr–Coulomb failure criterion. As observed, the breakout width tends to decrease with depth while breakout extent does not vary much, which is consistent with the BS-1 borehole observations in Fig. 2. This can be explained by the low slopes of calibrated stresses ($a_{S_{Hmax}}$ and $a_{S_{hmin}}$, with mean values 4.3 and 7.2 MPa/km, respectively; Fig. 10), which resemble well the experimental results in Valley and Evans[10]. All models converge towards a breakout orientation $\theta_b = 54°$, which is precisely the orientation of S_{hmin} reported in Valley and Evans[57]. Fig. 11 shows the 95 calibrated stresses and breakout geometries attained by using the Mogi–Coulomb failure criterion. Despite the overall trends of calibrated principal stresses are similar to those attained by using Mohr–Coulomb failure criterion, the envelope of the calibrated S_{Hmax} is now broader due to the strengthening effect of σ_2 (not accounted for by the Mohr–Coulomb failure criterion). This negative finding, as well as the strengths and weaknesses of the tested failure models will be further discussed in Section 6.

Fig. 12 shows the correlation at 3000 m MD between the input parameters S_{Hmax}, S_{hmin}, c, ψ, C_o, A and B and the borehole failure indicators w_{BO} and e_{BO} using the Mohr–Coulomb criterion. As observed, the correlation between S_{Hmax}, S_{hmin} and C_o is almost linear, which is consistent with the results shown in Section 4.3. As expected, the correlation between parameters and measurements is very low, which highlights the non-linearity of our formulation. As observed in Fig. 10, the initial sampling of the parameter space was nearly uniform (black versus grey lines), and the number of models fulfilling the posterior rejection criterion is large enough to draw meaningful
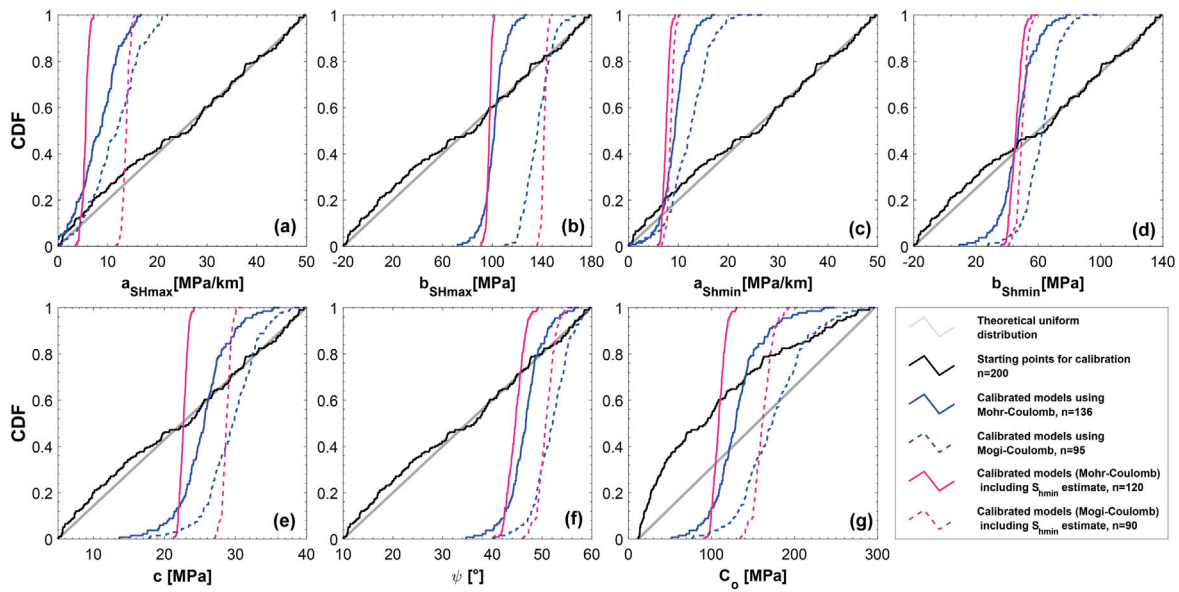
Fig. 10. Prior (black) and posterior cumulative density functions in the absence (blue lines) and in the presence (pink) of an estimate of S_{hmin} at a depth 4632 m MD: (a) slope of S_{Hmax}; (b) intercept of S_{Hmax}; (c) slope of S_{hmin}; (d) intercept of S_{hmin}; (e) cohesion, c; (f) internal angle of friction, ψ and (g) uniaxial compressive strength, C_o. (For interpretation of the references to colour in this figure legend, the reader is referred to the web version of this article.)

Table 2
Lower and upper bounds of calibrated S_{Hmax} and S_{hmin} using Mohr–Coulomb and Mogi–Coulomb failure criteria.

	Mohr–Coulomb		Mogi–Coulomb	
	Lower bound	Upper bound	Lower bound	Upper bound
$a_{S_{Hmax}}$ [MPa/km]	5.4	6.5	4.8	7.6
$b_{S_{Hmax}}$ [MPa]	87	130.2	138.6	230.5
$a_{S_{hmin}}$ [MPa/km]	7.5	4.5	6.5	7.6
$b_{S_{hmin}}$ [MPa]	31.31	87.5	30.6	124.5

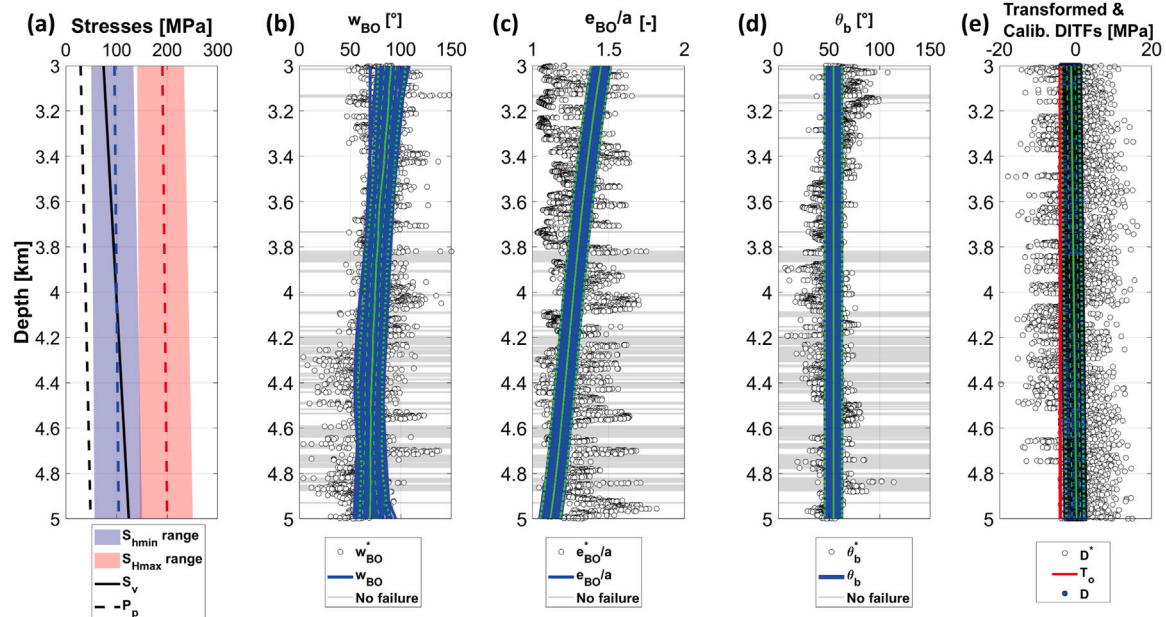**Fig. 11.** 1st order calibration outputs while using Mogi–Coulomb failure criterion. See the caption of Fig. 9 for further details.

statistical distributions regardless of the chosen failure criterion. The range of calibrated parameters is generally large (see Fig. 10 and Table 2), which again draws attention to the non-uniqueness of the inverse problem illustrated in Section 4.3. Non-uniqueness highlights
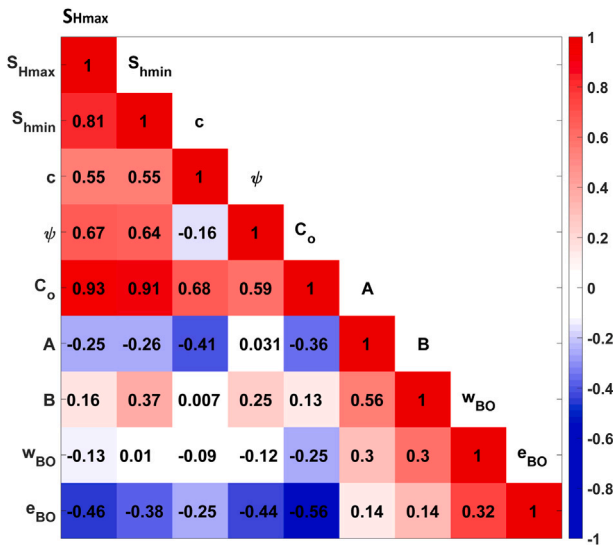
Fig. 12. Correlation matrix between the 1st order calibrated parameters S_{Hmax}, S_{hmin}, c, ψ, C_o, A and B and the borehole failure indicators w_{BO} and e_{BO}. Correlation coefficients are placed in the middle of each cell. The Mohr–Coulomb failure criterion and MD=3000 m were selected. Similar qualitative results are attained by using the Mogi–Coulomb failure criterion or any other given depth.

the inherent parametric uncertainties and can be alleviated by adding either more measurements of a given kind, or more kinds of measurements. In the context of this work, the impact of the number of measurements was done by skipping cross-sections. This exercise led to results almost identical to those in Figs. 9–11. In the next section, we explore how non-uniqueness can be alleviated by adding an additional type of measurement, i.e., S_{hmin} after the interpretation of a XLOT.

5.1.2. Reducing the solutions uncertainty

The best estimate of S_{hmin} from hydraulic stimulation was considered as a measurement[1] at a depth of 4632 m MD. The new measurement was added to the objective function F in Eq. (19). The first order calibration was carried out using the same 200 initial set of parameters as in the prior exercise. After applying the posterior rejection criterion based on the objective function value, only 120 and 90 models are selected when the Mohr–Coulomb and Mogi–Coulomb are used as failure criteria, respectively (136 and 95 in the absence of the S_{hmin} measurement). Figs. 13 and 14 show the dramatic reduction of uncertainty in the calibrated stress model parameters regardless of the considered failure criterion, as displayed by the narrower envelopes of plausible solutions. Interestingly, the use of the Mogi–Coulomb criterion leads to conceptually wrong stress profiles, which are inconsistent with the faulting regime data derived from the focal mechanisms of the microseismic events induced during hydraulic stimulation, i.e., not honouring the transitional regime at ca. 4800 m MD. Although this may be a plausible inference, we acknowledge that the kinematics of faulting represented by focal mechanisms is not always consistent with faulting mechanics represented by the stress state. Indeed, the Mohr–Coulomb criterion is, in the case of BS-1, more consistent, but this does not exclude the validity of the Mogi–Coulomb criterion. The Mogi–Coulomb failure criterion is nevertheless problematic in at least two other aspects. First, it yields calibrations that contravene bounds on admissible S_{Hmax} values imposed by frictional limits[10]. Second, it is not capable of reproducing, in the case of BS-1, the simultaneous observation of a decrease in breakout width and constant breakout extension with depth when using the Mogi–Coulomb criterion (Fig. 11). For these reasons, we use the Mohr–Coulomb criterion in further analyses.

The reduction of parametric uncertainties is best observed in Fig. 10. As observed, including one single measurement of S_{hmin} reduces drastically the range of calibrated parameters, as inferred from the steeper shape of all CDFs.

5.2. 2nd order calibration

The 1st order calibration presented so far yields practical insights on the general trends of both stress and strength along the borehole. These trends are representative of the mean conditions along the borehole, but are not capturing the variation around the mean. In natural systems like rock masses, such variations can be locally large. It is important to quantify this variability for the design of completion schemes including packers because such variability can cause locally conditions that are much more severe than the average conditions and that can cause completion problems. To fill this gap, the 2nd order calibration is carried out using as starting parameterization and prior information the 1st order parameter values leading to the median profile of S_{Hmax} in Fig. 9. Only one calibration is presented here for the sake of brevity. For the reason stated in Section 5.1, only the Mohr–Coulomb failure criterion is used. Each parameter intervening in model equations is now parameterized with pilot points regularly spaced every 10 m. The pilot point discretization is common to all strength and stress parameter profiles, which leads to an overall parameterization involving 1407 pilot points. Ordinary kriging was used as spatial interpolation algorithm to render continuous profiles from values at pilot points.

The results in terms of goodness of fit and derived parameters are displayed in Figs. 15 and 16, respectively. The 2nd order calibrated outputs (Fig. 15) resemble not only the trends observed in measurements, but also the corresponding small scale variabilities. The goodness of fit is striking, the root mean square errors being 10°, 0.086, 9° and 4.6 MPa for breakout width, normalized extent, orientation and DITFs, respectively (the initial misfits corresponding to the 1st order calibration were 27°, 0.175, 25° and 11.5 MPa). The 2nd order calibrated outputs reproduce well most of the small gaps without breakouts (shaded blue areas in Fig. 15a) and most of the maxima/minima of normalized extent (Fig. 15b). The extreme values along measured profiles are not exactly captured because (1) the number of pilot points, which exerts major control on computation effort, is not enough for that purpose, and (2) capturing the variability at the smallest scale would lead to undesired large (although perhaps realistic) oscillations in the profiles of calibrated parameters in Fig. 16. The derived parameters stress/strength in Fig. 16 are all plausible. The stress profiles of S_{Hmax} and S_{hmin} reproduce well the transitional regime at ≈4800 m depth reported by Valley and Evans[10]. The profiles of strength parameters in panels b to d display values coherent with those in the literature[10]. It is worth noting how the interplay between stress and strength is properly captured by the 2nd order model, i.e., there is a general negative correlation between the peaks of stress and strength at the gaps in the absence of breakouts (low stress/high strength or vice versa). The orientation of breakouts displays low departures (± 5°) from the median value of 144°, as reported in Häring et al.[1]. Finally, Shen's parameters defining our failure model are well within standard limits[58].

6. Discussion

6.1. Failure models evaluation

Our evaluation of failure models approach allows us to explore the validity of failure criteria and their ability to reproduce the borehole failure observations. In theory, models accounting for the strengthening effect of the intermediate principal stress – such as the Mogi–Coulomb criterion used in our study – capture more completely failure processes compared to models ignoring this effect (e.g. the Mohr–Coulomb
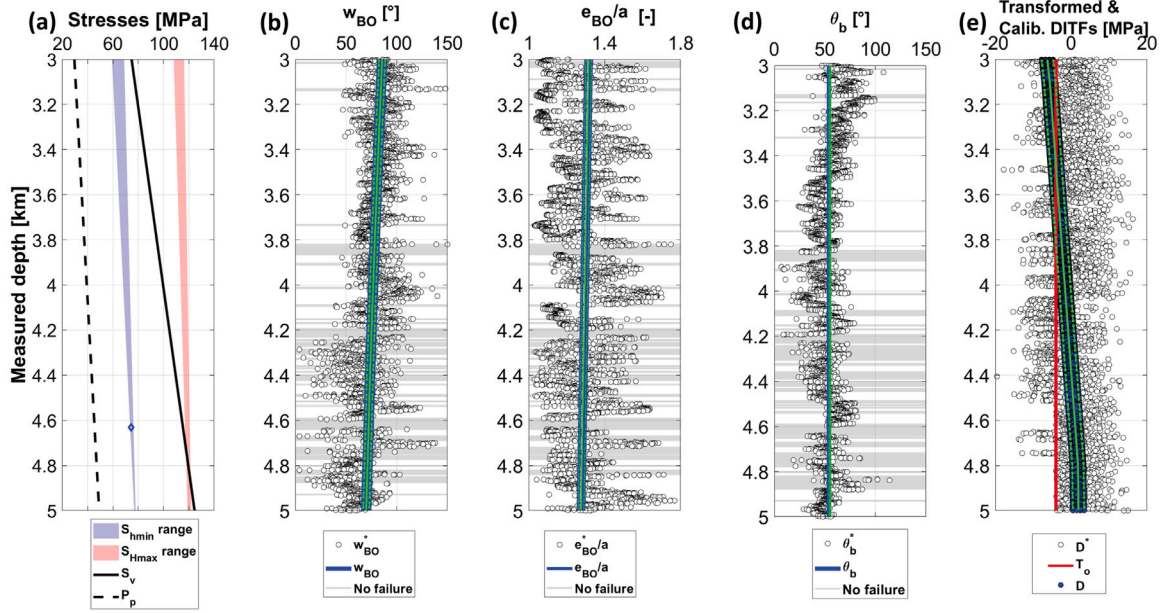
Fig. 13. 1st order calibration outputs in the presence of a new measurement of S_{hmin} considering the Mohr–Coulomb failure criterion. See the caption of Fig. 9 for further details.
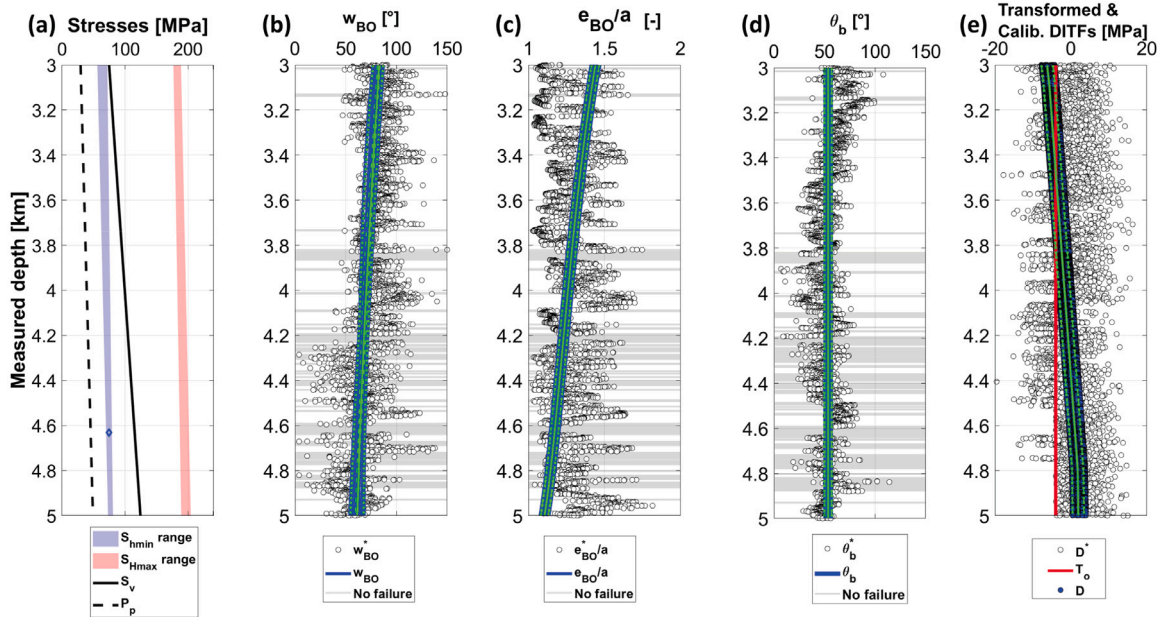

Fig. 14. 1st order calibration outputs in the presence of a new measurement of S_{hmin} considering the Mogi–Coulomb failure criterion. See the caption of Fig. 9 for further details.

criterion). However, our analyses show that calibration using the Mogi–Coulomb combined with an estimate of S_{hmin} magnitude from hydraulic tests leads to conceptually wrong stress profiles. Indeed, the obtained stress profiles (see Section 5.1.2) suggests a pure strike-slip stress regime ($S_{Hmax} > S_v$) while indications from focal mechanisms indicate a mix of strike-slip and normal faulting regimes ($S_{Hmax} \approx S_v$). Profiles obtained using the Mohr–Coulomb criterion are consistent with the stress regime observations, honouring the transitional regime at ca. 4800 m MD. These results are also in agreement with Valley and Evans[10]. Although this rationale is plausible, the kinematics of faulting represented by focal mechanisms is not always consistent with faulting mechanics represented by the stress state. Thus, choosing an "appropriate" failure criterion cannot be based solely on this observation.

When discussing the validity of the failure criterion, we shall recall that we used the Kirsch closed-form solution to compute stress because it is computationally attractive and is easy to implement. However, one must bear in mind its limitations. This analytical solution does not capture progressive failure and assumes that the initial breakout width remains constant once failure is initiated. Thus, this method tends to underestimate borehole failure parameters. Instead, the Mohr–Coulomb failure criterion tends to overestimate failure parameters because it neglects the strengthening effect of the intermediate stress effect. We assume that the Mohr–Coulomb criterion is performing well in our application because both conservative and non-conservative effects are compensating leading to stress and strength estimates that are consistent with independent stress observations, while combining the Mogi–Coulomb criterion with the analytical stress computation
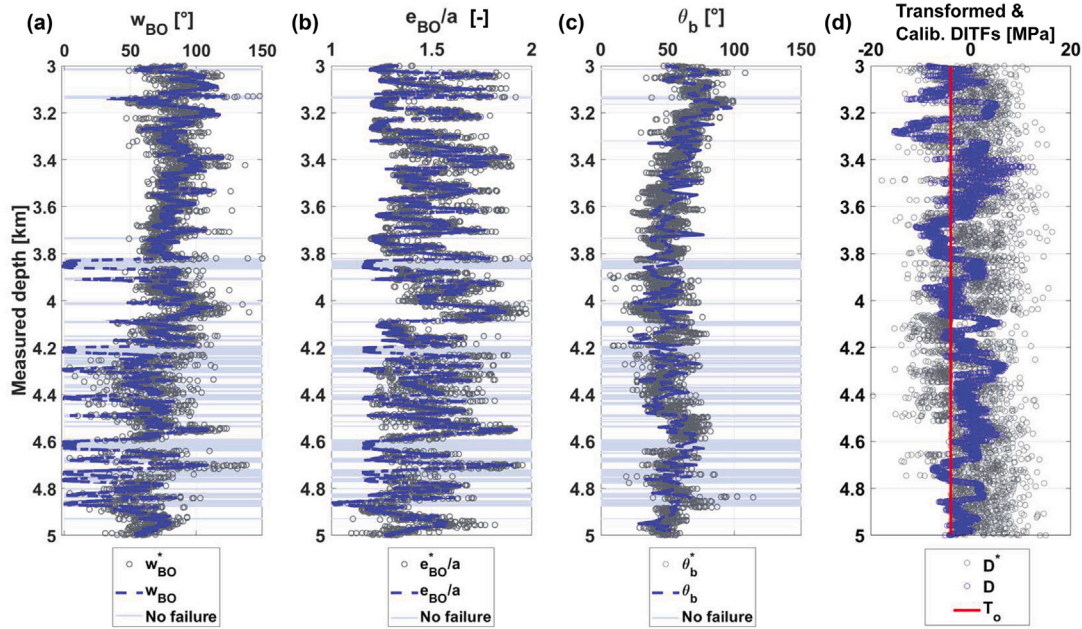
Fig. 15. Calibrated failure profiles using pilot points method from 3 to 5 km. (a) breakout width; (b) breakout extent; (c) breakout orientation; (d) Transformed and calibrated DITFs. In (a)–(c), the grey circles correspond to failure observations while in (e) they depict the estimated minimum hoop stress derived from DITFs observations. In (a)–(e), the dashed blue lines correspond to the calibrated failure using Mohr–Coulomb criterion. Light blue shaded areas in panels (a), (b) and (c) correspond to depths with no breakouts. The red line in panel (d) depicts the tensile strength, $T_o = -4$ MPa. (For interpretation of the references to colour in this figure legend, the reader is referred to the web version of this article.)
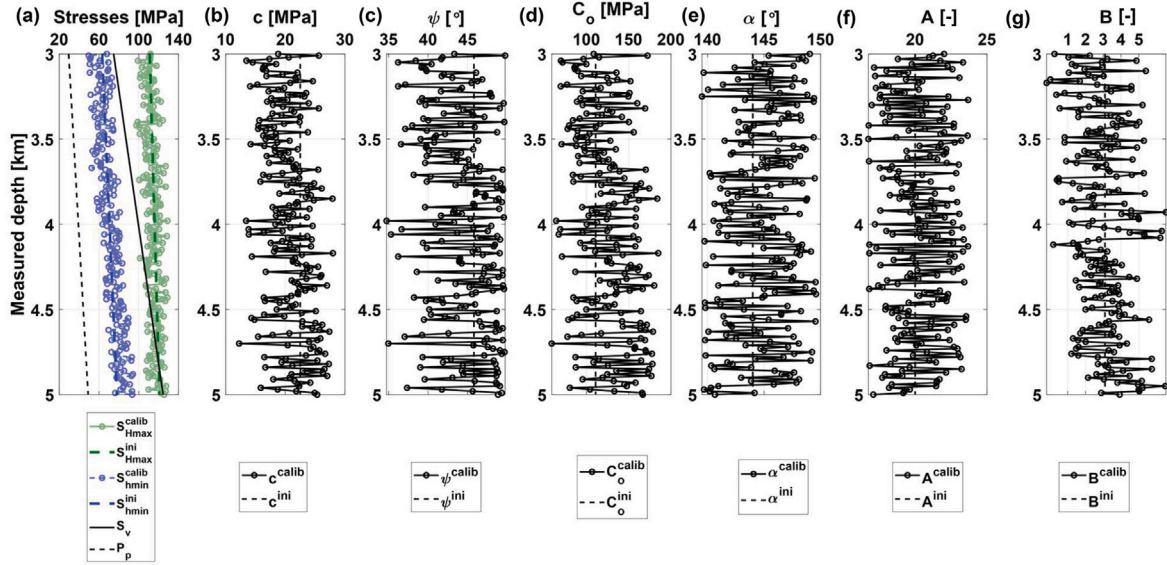

Fig. 16. Calibrated input parameters profiles using pilot points method from 3 to 5 km. (a) minimum and maximum principal horizontal stresses S_{Hmax} and S_{hmin}; (b) Cohesion; (c) internal friction angle; (d) uniaxial compressive strength; (e) the angle α of Euler and finally the regression parameters of Shen (f) A and (g) B. The dashed lines in all panels correspond to the initial depth profiles.

approach leads to an overestimation of the S_{Hmax} magnitude. Based on these results, we recommend to use the Mohr–Coulomb criterion in combination with the simple analytical stress computation which is used as standard in practice. Note that the limitation of analytical solutions not being able to reproduce progressive failure impairs also the computation of breakout extension. To solve this issue, we combined the analytical stress computation with the empirical relationship proposed by Shen[58]. We extended this relationship for complex stress state where we took into account borehole trajectory, mud pressure

and thermal stresses effect. When properly calibrated, this approach appears to be efficient at estimating breakout extension.

A path forward to develop the approach would be to make use of a more complex failure simulation, for example including continuum plasticity, continuum damage mechanics, hybrid continuum–discontinuum models. However these approaches involve a large number of unknowns, they are computationally demanding and we anticipate that they would be difficult to implement in the massive calibration framework we propose here. The use of empirical relationship supported by numerical simulation – as we apply here using
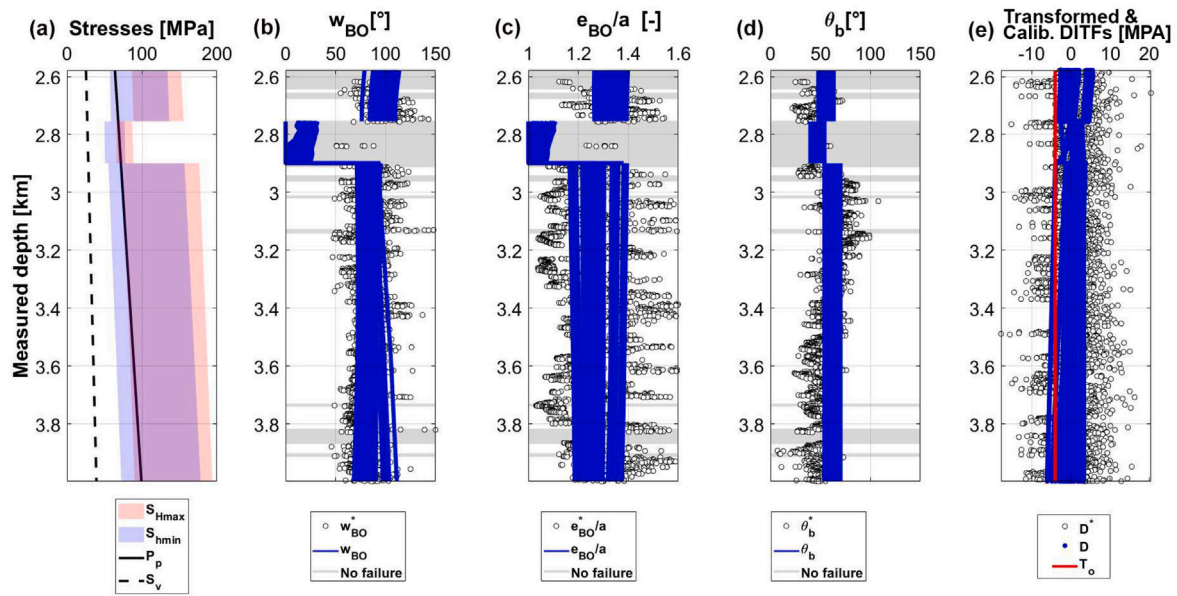
Fig. 17. 1st order calibration from 2578 m MD to 4000 m MD using the Mohr–Coulomb failure criterion performed for 100 different starting points. (a) the range of the calibrated S_{Hmax} (pink) and S_{hmin} (purple), S_v is plotted in solid black line and the pore pressure in dashed black line; Observed (black circles) and calibrated (blue lines) (b) breakout width; (c) normalized breakout extent; (d) breakout orientation; (e) transformed and calibrated DITFs. Grey lines in (b), (c) and (d) correspond to depths with no breakouts. The red line in (e) depicts the tensile strength $T_o = -4$ MPa. (For interpretation of the references to colour in this figure legend, the reader is referred to the web version of this article.)

the approach proposed by Shen[58] – is likely the most tractable and promising path forward to further develop our approach.

These limitations can be tackled by means of numerical models or more complex closed-form solutions. For instance, transient failure can be modelled by analytical solutions including continuum plasticity with non-associated flow rules and strain softening[33] or continuum damage mechanics[34] or by hybrid continuum–discontinuum models[35–37]. Unfortunately, the aforementioned approaches are either hard to parameterize using standard data sets, involve a larger number of unknown parameter and are computationally intensive, which precludes parameter estimation (See Section 2.6).

6.2. Sensitivity analyses

Sensitivity analysis were carried out prior to parameter calibration. Sensitivity analyses are useful to identify parameters with a significant impact on model outputs, and to bracket parameter ranges, thus reducing prior uncertainties and computational effort. The sensitivity analysis can help in selecting the parameters used in calibration. One key outcome of the sensitivity analyses is that the main parameters that influence borehole failure are S_{Hmax}, S_{hmin}, c, ψ, P_m in addition to Shen's parameters, A and B. We recognize that for practitioners, drilling mud density management is a primary tool to manage wellbore stability. However, mud weight is assumed to be constant in this paper ($\rho_m = 1.07$ g/cm^3) and the consideration of mud pressure on borehole stability is beyond the scope of this study. The aforementioned parameters were calibrated using PEST in order to reproduce the BS-1 borehole failure data. However, sensitivity to parameters controlling thermal stresses (i.e., Young Modulus, E, the coefficient of linear expansion, β and the Poisson ratio, ν) was not studied. This is justified by the fact that the thermal stresses are small compared to the mechanical stress when considering borehole breakouts. Thermal stresses are however often necessary to consider for explaining DITFs. The estimation of the relevant cooling magnitude occurring during drilling is also subject to uncertainties. We used a value proposed by Valley and Evans[10] to estimate thermal stresses and did not consider them as additional calibration parameters. The topic of the variability of thermo-elastic parameters on the wellbore failure could be further investigated.

6.3. Stresses trends with depth

Our 1st order model calibration provides insight into the depth trend of stress magnitudes. The outputs of the 1st order calibration are consistent with Valley and Evans[10] but the probabilistic model calibration proposed here allows to investigate a much broader possible solutions range and increases confidence in the stress characterization. A common feature of the calibrated S_{Hmax} and S_{hmin} profiles is the low gradient with depth. This explains why breakout width tends to decrease with depth in BS-1, although, solutions that reproduce equally the observations are non-unique. This problem was addressed by using regularization, information to bound and constrain input parameters as well as the available best estimate of S_{hmin} from hydraulic stimulation. The latter reduced significantly the solution uncertainty, which shows that it is very important to collect these data in order to constrain the posterior distribution of the calibrated parameters.

The geodynamic explanation of the observed low stress gradient remains uncertain. S_{hmin} also has a low gradient but this result is largely dependent on the assumed cooling profile for the formation of DITFs. Valley and Evans[10] showed that considering a much lower cooling profile in the upper section of the well can increase the S_{hmin} gradient by to up to 12 MPa/km, but not more. Another possible explanation is that the stiffness contrast may affect the stress gradient. An alternate explanation hypothesized by Valley and Evans[10] is that the observed reduction of horizontal stress gradient would require a tectonic strain gradient, with more intense straining at the cover basement interface and a reduction of the tectonic straining with depth.

In addition to the decrease in depth of breakouts width, we observe that they are continuous except for a large gap from 2747 m TVD to 2899 m TVD and some other minor gaps below (Fig. 2). These borehole segments coincide with those of strong intensity of natural fractures. We have been interested in studying this paradox. In order to get the stress and strength depth profiles in this fractured zone, we run a 1st order calibration from 2578 m MD to 4000 m MD. The studied depth interval were divided into 3 different zones: (1) from 2578 to 2758 m MD, (2) from 2758 to 2900 m MD and finally (3) from 2900 to 4000 m MD. In each zone, 7 parameters are calibrated (S_{Hmax}, S_{hmin}, α, c, ψ, A and B (Fig. 18) and the prior distribution of each parameter is randomly sampled assuming a uniform distribution, which

renders overall 100 initial parameterizations that explore the global parameter space. Fig. 17 shows the calibrated stresses and failure depth profiles. We notice that stresses magnitudes in 'zone 2' are smaller than in 'zone 1' and 'zone 3' and more importantly, the conditions in 'zone 2' approaches isotropic stress conditions ($S_{hmin} \approx S_{Hmax} \approx S_v$). In unfractured zones (zone 1 and 3), S_{Hmax} varies between 102 and 113 MPa, S_{hmin} varies in the range [80.5–90.9 MPa] and S_v is approximately equal to 70 MPa. In the fractured zone (Zone 2), $S_{Hmax} \approx 88$ MPa, $S_{hmin} \approx 69$ MPa). The maximum stress difference thus decreases from 43 MPa (zone 1 and 3) to 18 MPa (zone 2). As we have almost no breakouts in zone 2, our calibration leads to a strength increase compared to the one in zones 1 and 3 (C_o varies between 115 and 119 MPa in zones 3 and 1 respectively, whereas it is around 137 MPa in zone 2). The fact that 'zone 2' is mainly affected by fractures and has almost no breakouts may be explained by a perturbed stress state in this zone, either as a remanence of pre-sedimentation exhumation and relaxation or in response to more recent tectonic loading. The fractured rock mass being softer, the stress level and differential stress may be lower which could explain the absence of breakouts.

6.4. Failure variability and implication for rock mass models

Wellbore failure variability is common and has been used to characterize stress heterogeneity[93–97]. Variations in breakout orientation gives a direct estimate of the stress orientation variability. However, an estimation of stress magnitude heterogeneity is more difficult to derive since it requires an independent estimate of strength. With our 2nd order calibration methodology, we can investigate the potential source of observed borehole breakouts variability and quantify in-situ the potential magnitude of stress and strength variability. Two end-members rock mass models can potentially explain the observed failure variability:

1. The failure variability arises primarily from the variability in stress orientation and magnitudes within a rock with relatively constant strength. A credible explanation for the stress variability is the stress perturbations associated with fracture slip. Studies of wellbore failure variation around fractures have been shown to be related to fracture slip[57,93].
2. The failure variability arises primarily due to variability in rock strength. In crystalline basements, like in the BS-1 borehole, strength variability could be associated with alteration related to hydrothermal fluid circulations. Velocity profiles derived from sonic logging shows variability[98] that could be related to strength and stiffness rock variability, although variation in stresses could also explain velocity variations.

These two rock mass models are not incompatible, and it is not unlikely that both stress and strength variations occurs concomitantly. We investigated these scenarios by performing 2nd order calibrations where only the stress parameters are calibrated while the strength parameters are assumed to be constant (Fig. 19) and here only strength parameters are calibrated and with no stress variability (Fig. 20). In both cases, the failure variability can be reproduced satisfyingly.

The histograms of Fig. 21 illustrate the variability distributions of stress and strength parameters for these two scenarios as well as for a case where both strength and stress parameters are calibrated concomitantly. The coefficient of variations (COV) for strength parameters are 20% and 13% for cohesion and friction, respectively. Such values are not surprising and correspond to the variability obtained from data compilation from testing programmes on igneous rocks[99]. A variability in stress of 7 to 8 MPa (1σ) is observed when strength parameters are assumed to be constant. Comparing these standard deviations with absolute stress magnitude in the range of 80 MPa for S_{hmin} and 105 MPa for S_{hmax} lead to a maximum COV for the stress

parameters of about 10%. Such values can be easily explained by stress variability induced by fracture slip (e.g. Valley et al.[100]). Thus our observations and analyses are consistent with both the proposed source of failure variations (strength or stress heterogeneity) and it is likely that both sources act concomitantly at inducing failure parameters variability. However, it is important that considering only strength variability while assuming that stresses are linear trends in depth does not explain neither the variability of the breakout orientation nor the DITFs. Our analyses provide however a unique opportunity to quantify in-situ the magnitude of the stress and strength variability.

6.5. Limitations and applicability of the methodology

The novel methodology described above proved very efficient on the BS-1. Its mathematical formulation (see Section 2) is generic and applicable to any case study. However, as any new method, if suffers from some limitations. In this section, we summarize them and provide some ongoing footsteps to overcome them. One of the main novelties of our methodology is the inclusion of breakout extent in the calibration process. Breakout extent has been traditionally neglected because its computation is difficult. Theoretical considerations and experimental observations suggest that breakouts develop by progressive failure, i.e., incremental evolution of the borehole shape characterized by a fairly stable breakout width and an increasing extent (e.g., Zoback et al.[5]). Solving progressive borehole failure requires complex numerical simulations including, e.g., viscoplastic constitutive laws, which are not tractable in a calibration process often demanding a large number of iterations. However, breakout extent is a very important parameter because it addresses the suitability of borehole segments for zonal isolation, i.e., for packer location. To overcome this impasse, we use an empirical approach (see Section 2.4). Possible improvements involve more complex mathematical approaches, e.g., the semi-analytical approach proposed by Setiawan and Zimmerman[101].

Dealing with the absence of borehole breakouts is also difficult. The absence of breakouts indicates that failure conditions have not been met at the borehole wall, but do not provide insights on how far from failure is the stress–strength state. This often lead to difficulties in the calibration process, which tends to yield stress conditions at the borehole wall close to failure, even in the absence of breakouts. We did not encounter this problem in the case of the BS-1 dataset because breakouts are pervasive (81% of the borehole length) and sufficient information is available for constraining the calibrated solutions. However, we envisage ill-posed inverse problems in case studies with limited occurrence of breakouts. A possibility to overcome this problem consists of adding a penalty criterion to the objective function (Eq. (18)) that accounts for discontinuous or boolean variables (presence/absence of breakouts, i.e., failure or not). Unfortunately, boolean variables are not well-suited for constraining calibration and equivalent continuum criteria should be used instead. The same occurs with the evaluation of DITFs. In that case, we calculate the minimum hoop stresses leading to the presence/absence of DITFs. A similar criterion, taking into account stress and strength parameters can be used to account for the presence/absence of breakouts.

The BS-1 borehole is essentially sub-vertical. In principle, the use of data out of deviated boreholes should not pose any additional difficulty. In fact, the combination of boreholes with different orientations should increase both quantitatively and qualitatively the calibration constraints and yield better solutions. In fact, the robustness and applicability of the suggested methodology is being tested at present.

The sensitivity to parameters controlling thermal stresses (i.e., the Young Modulus, the coefficient of linear expansion and the Poisson ratio) has not been analysed yet, which was justified by the relative low presence of DITFs in borehole BS-1. In this line of arguments, the impact of the heterogeneity of thermo-elastic parameters on wellbore failure should be further investigated. Finally, it is important
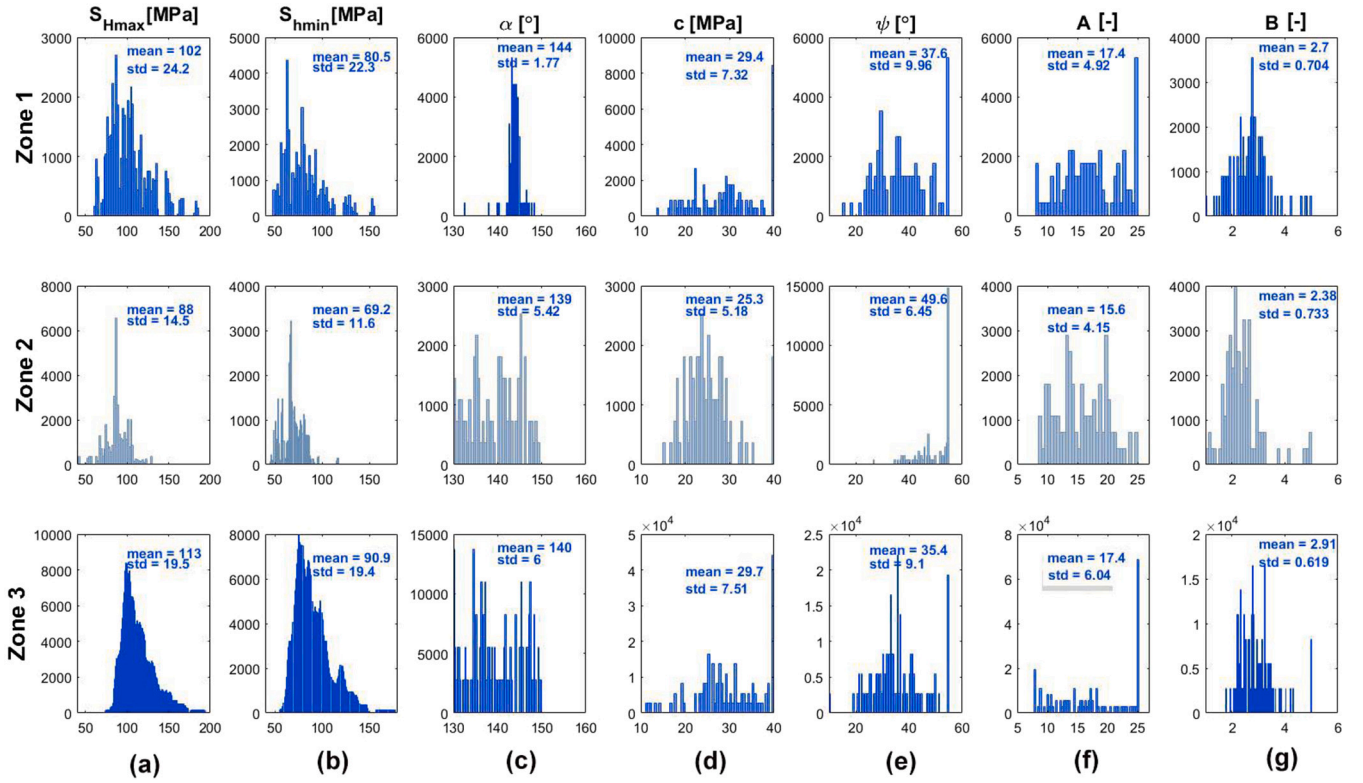
Fig. 18. Histograms of the calibrated parameters (plotted in columns) in each of the three considered zones (rows). (a) maximum horizontal principal stress, S_{Hmax}; (b) minimum horizontal principal stress, S_{hmin}; (c) Euler's angle, α; (d) cohesion, c; (e) internal friction angle, ψ; (f) Shen's parameters, A and (g) B.
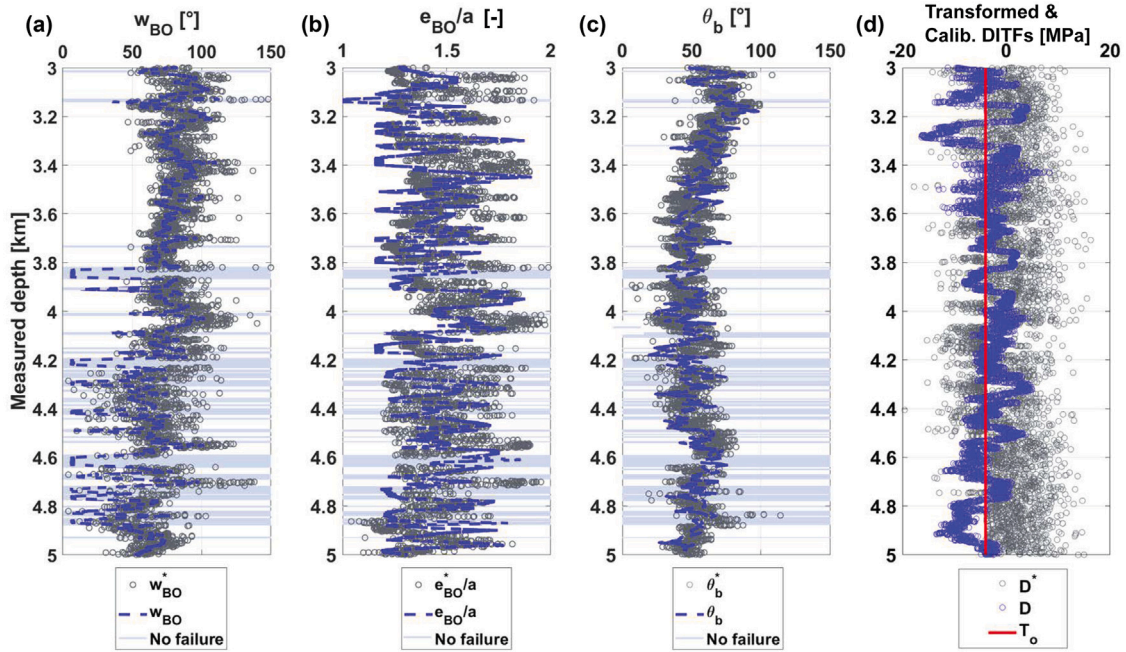

Fig. 19. Calibrated failure profiles for the first scenario where it is assumed that breakouts and DITFs variability comes from variability among stresses only. See the caption of Fig. 15 for further details.

to highlight that our approach is based on the inversion of principal stresses at the borehole wall. The concomitance of low internal well pressure (quasi hydrostatic) and the in-situ stresses in BS-1 favour the tangential stress as the maximum principal stress. However, this may not be the case in practice and particular breakout geometries may be generated[102] that are hard to cope with the suggested methodology.

Similarly, stress–strength situations in which breakouts initiate with large width (> 90°) often lead to total borehole collapse and the formation of washouts[5]. Such special situation would also lead to difficulties in applying our inversion approach.
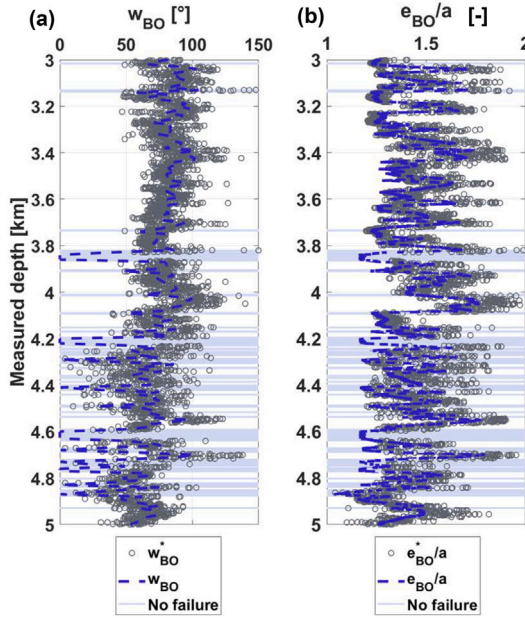
Fig. 20. Calibrated failure profiles for the second scenario where it is assumed that breakouts variability comes from variability among rock strength only. See the caption of Fig. 15 for further details.

7. Conclusions

In state-of-the-art wellbore failure analyses, stresses and strength properties are commonly estimated separately. Given the limitations of the traditionally used approaches, we proposed in this paper a new methodology to jointly evaluate the stress tensor components and orientations, and the rock strength properties (e.g. cohesion, friction) in a robust probabilistic framework. For this purpose, analytical and empirical solutions for estimating wellbore stresses and failure parameters were combined with the regularized pilot points method as implemented in the PEST software. We used measurements which are

available during or shortly after drilling, i.e., breakout width, breakout extent and breakout orientation at different depths in addition to the presence/absence of DITFs (including both axial and en-echelon tensile fractures, A-DITFs and E-DITFs). In addition, measurements of estimated parameters can be easily included in a generic manner (e.g., S_{hmin} interpreted from XLOT, etc.). Also, all stress components around the borehole, including the remnant thermal stresses arising from the cooling of the borehole wall were accounted for. For illustration purposes, the proposed methodology was applied to the extensive borehole data set along the 2.5 km crystalline section of the borehole BS-1, in Basel (Switzerland). Our failure analyses approach and its application to the data set from the BS-1 borehole allow us to improve our understanding of failure processes in boreholes, the relationship amongst failure parameters and to better understand the stress and strength conditions and their variability in the earth crust:

- Breakout width is commonly analysed to estimate the in-situ stress state while breakout extension is considered to be ineffective for such purpose and thus largely neglected. In this paper, we investigated in more details borehole failure by using not only breakout width for stress and strength estimation but also breakout extent, breakout orientation and the presence or absence of DITFs. Using data from the deep geothermal well BS-1, shows that width and extent of failure are non-linearly related. This can be explained by considering the relationships between stress concentration at the borehole wall and material strength.

- Based on the observed relationships between width and extent of failure, we developed a new approach by extending Shen's empirical relationship[58] to cover wellbore conditions that include internal well pressure, pore pressure and thermo-elastic stress and apply it considering the Mohr–Coulomb and Mogi–Coulomb failure criteria. This approach provides an effective and computationally efficient way for analysing the extent of failure.

- The joint inversion of stress and strength parameters proposed in our approach lead to a non-unique solution for the strength and stress profiles. This problem was addressed by using singular value decomposition and regularization, information to bound input parameters and the available measure of S_{hmin} from hydraulic stimulation. The latter reduced significantly the solutions uncertainty, which shows the importance of collecting such data.
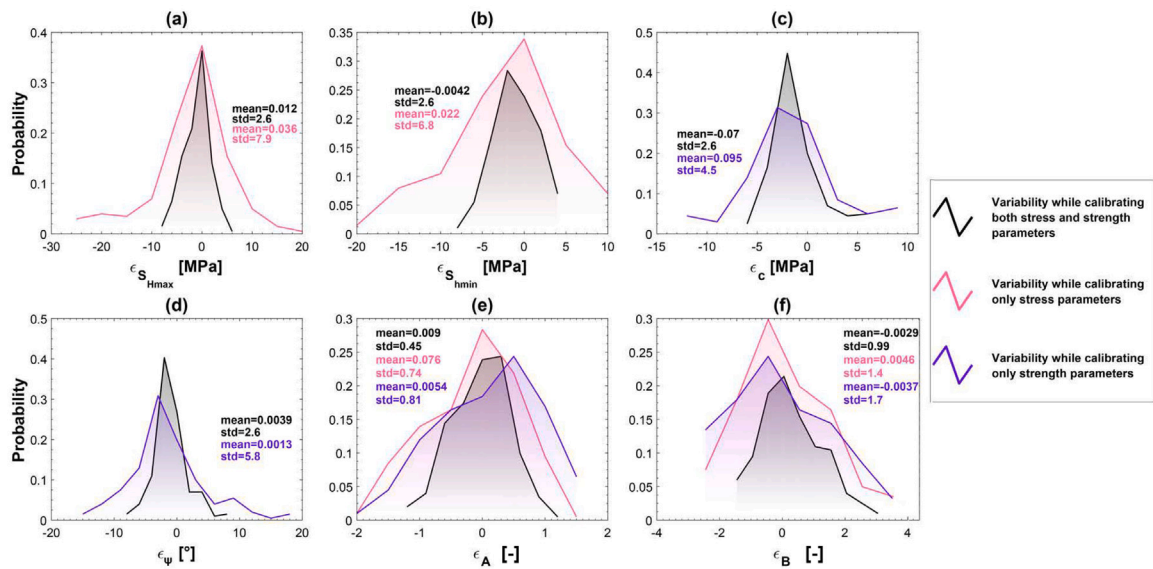

Fig. 21. Histograms of parameters variability, $\epsilon_{i,zi}$, for three different scenarios assuming that failure variability is due to (1) both stress and strength variability in depth (black shaded histograms), (2) stress variability only, (3) rock heterogeneity only. These shaded histograms show the probability on the y axis and the bins centres on the x axis of (a) S_{Hmax}; (b) S_{hmin}; (c) cohesion, c; (d) internal friction angle, ψ and finally Shen's parameters (e) A and (f) B. (For interpretation of the references to colour in this figure legend, the reader is referred to the web version of this article.)

- We show that in the framework of the simplified stress computation using an elastic solution around a cylindrical opening[19], the Mohr–Coulomb criterion provides the stress profiles the most consistent with independent observation.
- The obtained stress profiles present systematically low stress gradients which confirms the results of Valley and Evans[10] obtained within a less systematic parameter estimation framework. The geodynamic explanation for such low stress gradients remains uncertain but could be attributed to non-uniform tectonic straining associated with decoupling at the basement–cover interface.
- The absence of breakouts along certain segments of BS-1 is consistently associated with increased natural fracturing. We analysed this situation with our parameter estimation approach and showed that the absence of failure requires a reduction of the differential stress with a stress state tending towards isotropic conditions. These stress conditions can be explained by stress relief and rock mass softening associated with fracturing. In the upper crystalline section of the borehole, near the basement–cover interface, such stress relief and fracturing could be associated with the near surface exhumation that took place in carboniferous and permian times.
- Our 2nd order analyses suggest that both strength and stress heterogeneity likely contribute concomitantly to the observed borehole failure variability. We provide a unique in-situ quantification of strength and stress parameters. The COV for frictional parameters is about 13% and 20% for cohesive strength parameters. The COV for stress magnitude variations is about 10%. However, the variability of the strength only while assuming that the stresses are linear functions of depth, is not sufficient to explain the variability in depth of both DITFs and breakout orientation.
- The wellbore failure analyses approach presented in this paper sets the base for quantitative wellbore failure prediction and risk analyses that are required for the design and deployment of innovative borehole completions enabling zonal isolation that are required for unlocking the potential of deep Engineered Geothermal Systems (EGS).

Declaration of competing interest

Acknowledgments

Appendix A. Stresses transformation to a local borehole Cartesian coordinate system

This section contains the necessary mathematical background that we have used to compute the stress around a wellbore arbitrarily oriented to the principal stress directions. The general approach was presented in Peška and Zoback[103] and initially developed by Hiramatsu and Oka[104]. We have been interested in developing that solution here again because it is of key importance for most of the work done on wellbore failure analysis. Let the far-field stress he expressed by means of the principal stresses S_1, S_2, and S_3. Then the stress state is fully described by the tensor $\mathbf{S}_{lmn}$ and three angles α, β, γ:

$$\mathbf{S}_{lmn} = \begin{pmatrix} S_1 & 0 & 0 \\ 0 & S_2 & 0 \\ 0 & 0 & S_3 \end{pmatrix} \tag{A.1}$$

where $S_1 > S_2 > S_3$ are the principal stress magnitudes. The angles α, β, γ are called Euler angles. They define the orientations of the principal stresses axes $(\vec{l}, \vec{m}, \vec{n})$ with respect to the geographic coordinate system $(\vec{x}, \vec{y}, \vec{z})$, with $\vec{x}$ pointing to the North, $\vec{y}$ pointing to the East and $\vec{z}$ pointing downward.

Euler angles α, β, γ define a sequence of three rotations that must be used in order to rotate principal stresses axes $(\vec{l}, \vec{m}, \vec{n})$ to the geographic coordinate system $(\vec{x}, \vec{y}, \vec{z})$. During this rotations sequence, $(\vec{x}, \vec{y}, \vec{z})$ is rotated through two intermediate systems $(\vec{x}_1, \vec{y}_1, \vec{z}_1)$ and $(\vec{x}_2, \vec{y}_2, \vec{z}_2)$. The first rotation is the positive rotation α (counterclockwise) with respect to the axis $\vec{z}$ ($\alpha \in [0° \ 360°]$) using the matrix $\mathbf{R}_z$ (Eq. (A.2)). After this rotation, we get to the first intermediate axis $(\vec{x}_1, \vec{y}_1, \vec{z}_1)$ where $\vec{z}_1 = \vec{z}$. Then, comes a positive rotation β around $\vec{y}_1$ ($\beta \in [-90° \ 90°]$) using the matrix $\mathbf{R}_{y_1}$ (Eq. (A.3)). We obtain then the second intermediate coordinate system $(\vec{x}_2, \vec{y}_2, \vec{z}_2)$ where $\vec{y}_2 = \vec{y}_1$. Finally, the positive rotation γ around $\vec{x}_2$ ($\gamma \in [0° \ 360°]$) by applying the matrix $\mathbf{R}_{x_2}$ (Eq. (A.4)) which gives us a final coordinate system that coincides with the principal stresses axes $(\vec{l}, \vec{m}, \vec{n})$ (Fig. A.1).

$$\mathbf{R}_z = \begin{pmatrix} \cos\alpha & \sin\alpha & 0 \\ -\sin\alpha & \cos\alpha & 0 \\ 0 & 0 & 1 \end{pmatrix} \tag{A.2}$$

$$\mathbf{R}_{y_1} = \begin{pmatrix} \cos\beta & 0 & -\sin\beta \\ 0 & 1 & 0 \\ \sin\beta & 0 & \cos\beta \end{pmatrix} \tag{A.3}$$

$$\mathbf{R}_{x_2} = \begin{pmatrix} 1 & 0 & 0 \\ 0 & \cos\gamma & \sin\gamma \\ 0 & -\sin\gamma & \cos\gamma \end{pmatrix} \tag{A.4}$$

Mathematically, this transformation is expressed as:

$$\mathbf{S}_{xyz} = \mathbf{R}_{lmn}^T \mathbf{S}_{lmn} \mathbf{R}_{lmn} \tag{A.5}$$

where $\mathbf{S}_{xyz}$ is the stress state in the referential coordinate system and $\mathbf{R}_{lmn}$ is the product of three rotations that make use of Euler angles.

$$\mathbf{R}_{lmn} = \mathbf{R}_z \mathbf{R}_{y_1} \mathbf{R}_{x_2} \tag{A.6}$$

$$\mathbf{R}_{lmn} = \begin{pmatrix} \cos\alpha\cos\beta & \sin\alpha\cos\beta & -\sin\beta \\ \cos\alpha\sin\beta\sin\gamma - \sin\alpha\cos\gamma & \sin\alpha\sin\beta\sin\gamma + \cos\alpha\cos\gamma & \cos\beta\sin\gamma \\ \cos\alpha\sin\beta\cos\gamma + \sin\alpha\sin\gamma & \sin\alpha\sin\beta\cos\gamma - \cos\alpha\sin\gamma & \cos\beta\cos\gamma \end{pmatrix} \tag{A.7}$$

A borehole coordinates system is defined $(\vec{u}, \vec{v}, \vec{w})$ (Fig. A.2) in order to describe the state of stress around a borehole. $\vec{w}$ runs along the borehole axis pointing downwards, $\vec{v}$ is a horizontal axis in the plane perpendicular to the borehole axis $\vec{w}$ and $\vec{u}$ comes out of the screwdriver rule. The borehole coordinate system is defined by two angles: (1) the borehole azimuth δ comprised in the interval $[0° \ 360°]$ and (2) the inclination of the borehole with respect to verticality Φ while $\Phi \in$
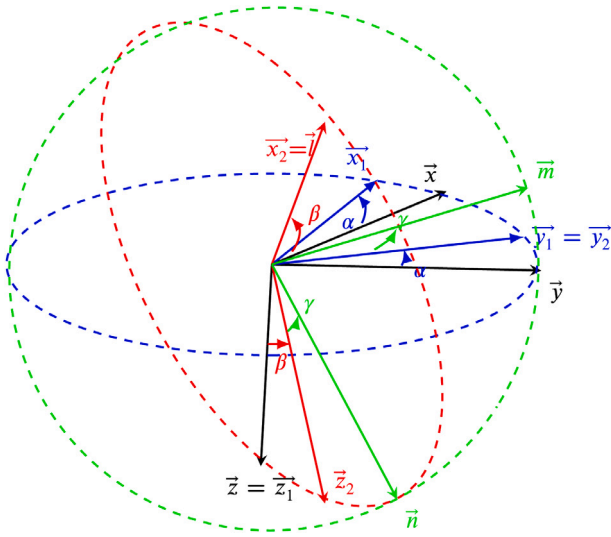
Fig. A.1. A sequence of three rotations to rotate the geographical system coordinate $(\vec{x}, \vec{y}, \vec{z})$ shown in black to the principal stresses coordinate system $(\vec{l}, \vec{m}, \vec{n})$ shown in green. This sequence rotates through two intermediate coordinate systems $(\vec{x}_1, \vec{y}_1, \vec{z}_1)$ (in blue) and $(\vec{x}_2, \vec{y}_2, \vec{z}_2)$ (in red). The first rotation α is around $\vec{z}$, the second is β around $\vec{y}_1$ and the last one is γ around $\vec{x}_2$. (For interpretation of the references to colour in this figure legend, the reader is referred to the web version of this article.)

$[0°\ 90°]$. The natural state of stress in the borehole coordinates system $\mathbf{S}_{uvw}$ is given as following:

$$\mathbf{S}_{uvw} = \mathbf{R}_{uvw}\mathbf{S}_{xyz}\mathbf{R}_{uvw}^T \tag{A.8}$$

where:

$$\mathbf{S}_{uvw} = \begin{pmatrix} S_u & S_{uv} & S_{uw} \\ S_{vu} & S_v & S_{vw} \\ S_{wu} & S_{wv} & S_w \end{pmatrix} \tag{A.9}$$

$\mathbf{R}_{uvw}$ is the direction cosine of $(\vec{u}, \vec{v}, \vec{w})$ relative to $(\vec{x}, \vec{y}, \vec{z})$, which can be expressed as the product of two rotation matrices $\mathbf{R}_\delta$ (counter-clockwise rotation of δ around $\vec{z}$) and $\mathbf{R}_\Phi$, (counterclockwise rotation of Φ around $\vec{y}$ (pointing to the East)):

$$\mathbf{R}_\delta = \begin{pmatrix} \cos\delta & \sin\delta & 0 \\ -\sin\delta & \cos\delta & 0 \\ 0 & 0 & -1 \end{pmatrix} \tag{A.10}$$

$$\mathbf{R}_\Phi = \begin{pmatrix} -\cos\Phi & 0 & -\sin\Phi \\ 0 & -1 & 0 \\ \sin\Phi & 0 & -\cos\Phi \end{pmatrix} \tag{A.11}$$

$$\mathbf{R}_{uvw} = \mathbf{R}_\Phi\mathbf{R}_\delta = \begin{pmatrix} -\cos\delta\cos\Phi & -\sin\delta\cos\Phi & \sin\Phi \\ \sin\delta & -\cos\delta & 0 \\ \cos\delta\sin\Phi & \sin\delta\sin\Phi & \cos\Phi \end{pmatrix} \tag{A.12}$$

Combining both Eqs. (A.5) and (A.9) gives us a direct expression between the principal stresses coordinate system $(\vec{l}, \vec{m}, \vec{n})$ and the borehole coordinate system $(\vec{u}, \vec{v}, \vec{w})$:

$$\mathbf{S}_{uvw} = \mathbf{R}_{uvw}\mathbf{R}_{lmn}^T\mathbf{S}_{lmn}\mathbf{R}_{lmn}\mathbf{R}_{uvw}^T \tag{A.13}$$

Appendix B. Stress perturbation induced by a cylindrical opening (Kirsch solution)

When a volume or rock is excavated, for example by drilling it, the state of stress around the excavation is modified. The equations that describe the elastic stresses around the hole in an infinite plate in one directional tension are generally referred to as the Kirsch solution[19] and are one of the most useful solutions in rock mechanics. This solution is often used to approximate the stress redistribution around deep boreholes and tunnels. The total stress around a filled borehole of radius a, in cylindrical coordinates (r, θ, w), and with an internal fluid at a pressure P_w, is given by Kirsch equations as following:

$$\mathbf{S}_{r\theta w} = \begin{pmatrix} S_{rr} & S_{r\theta} & S_{rw} \\ S_{\theta r} & S_{\theta\theta} & S_{\theta w} \\ S_{wr} & S_{w\theta} & S_{ww} \end{pmatrix} \tag{B.1}$$

where:

$$S_{rr} = \left(1 - \frac{a^2}{r^2}\right)\left(\frac{S_u + S_v}{2}\right) + \left(1 + \frac{3a^4}{r^4} - \frac{4a^2}{r^2}\right)\left(\frac{S_u - S_v}{2}\right)\cos 2\theta$$
$$+ \left(1 + \frac{3a^4}{r^4} - \frac{4a^2}{r^2}\right)S_{uv}\sin 2\theta + P_w\left(\frac{a^2}{r^2}\right) + S_r^{\Delta T} \tag{B.2}$$

$$S_{\theta\theta} = \left(1 + \frac{a^2}{r^2}\right)\left(\frac{S_u + S_v}{2}\right) - \left(1 + \frac{3a^4}{r^4}\right)\left(\frac{S_u - S_v}{2}\right)\cos 2\theta$$
$$- \left(1 + \frac{3a^4}{r^4}\right)S_{uv}\sin 2\theta - P_w\left(\frac{a^2}{r^2}\right) + S_\theta^{\Delta T} \tag{B.3}$$

$$S_{ww} = S_z - 4v\frac{a^2}{r^2}\left(\frac{S_u - S_v}{2}\right)\cos 2\theta - 4v\frac{a^2}{r^2}S_{uv}\sin 2\theta + S_w^{\Delta T} \tag{B.4}$$

$$S_{r\theta} = -\left(1 - \frac{3a^4}{r^4} + \frac{2a^2}{r^2}\right)\left(\frac{S_u - S_v}{2}\right)\sin 2\theta$$
$$+ \left(1 - \frac{3a^4}{r^4} + \frac{2a^2}{r^2}\right)S_{uv}\cos 2\theta \tag{B.5}$$

$$S_{rw} = \left(1 - \frac{a^2}{r^2}\right)\left(S_{vw}\sin\theta + S_{uw}\cos\theta\right) \tag{B.6}$$

$$S_{\theta w} = \left(1 + \frac{a^2}{r^2}\right)\left(S_{vw}\cos\theta - S_{uw}\sin\theta\right) \tag{B.7}$$

v is the Poisson's ratio. The subscripts (u, v, w) refer to the total stresses given in the local borehole coordinate system as in Eq. (A.9). $S_r^{\Delta T}$, $S_\theta^{\Delta T}$, $S_w^{\Delta T}$ are thermo-elastic stress components estimated by Eqs. (1) and (2).

Appendix C. Overview of the minimization algorithm implemented in PEST

We perform our calibration using PEST (Parameter ESTimation), a widely used code in environmental modelling to calibrate models and to determine uncertainty associated with parameters and predictions. PEST uses a nonlinear estimation technique known as the Levenberg–Marquardt (LM) method also known as the damped least-squares (DLS) method. It is used to solve non-linear least squares problems. This algorithm is used in many software applications for solving generic curve-fitting problems. For linear models, optimization is achieved in one step. However, for non-linear problems, parameter estimation is an iterative process. The Gaussian–Marquardt–Levenberg algorithm adjusts parameter values based on the derivatives of the observations with respect to the parameters (i.e., sensitivity or Jacobian matrix)[18].

Let us assume that the user has a specified model f. The Levenberg Marquardt algorithm performs a curve fitting on a given data set, by finding the optimum function parameters b that minimizes the sum of the squares of the deviations:

$$S(b) = min\left(\sum_{i=1}^{m}(y_i - f(x_i, b))^2\right) \tag{C.1}$$

where y_i are the target values, f, the output of the user's model, x_i, input values and b are the estimated parameters.

Let us assume that we have a model, X, and input parameters, b, such as principal stresses, S_{Hmax}, S_{hmin}, S_v. The action of the model (X) on the inputs in (b) produces a set of outputs (c) (w_{BO}, e_{BO}, θ_b and D in our case). Conceptually, the inputs react with each parameter to produce results. This can be formulated in the following equation[18]:
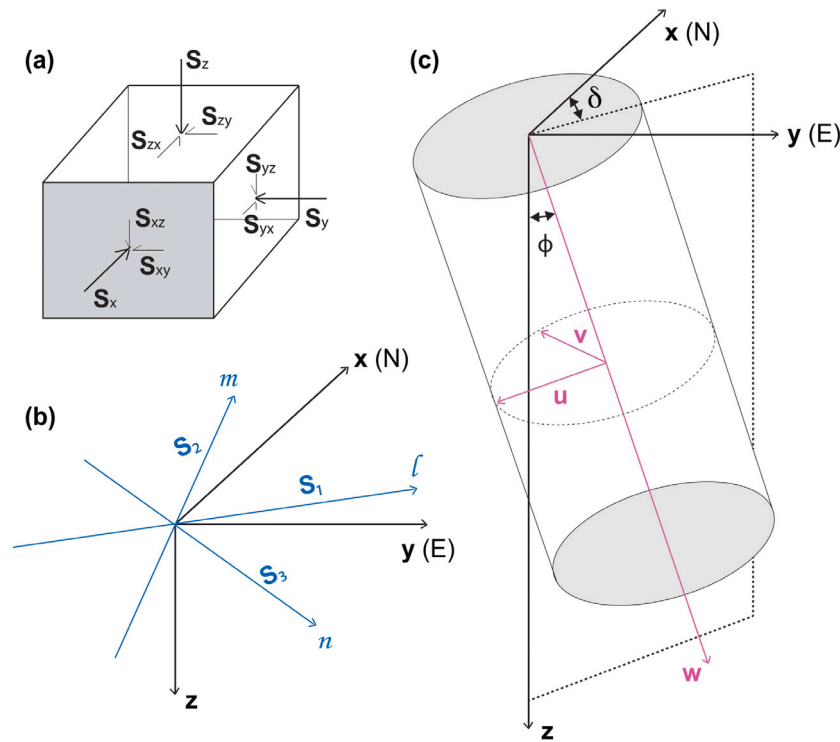
$$Xb = c \tag{C.2}$$

Fig. A.2. (a) Definition of stress tensor in arbitrary cartesian coordinates system. (b) reference geographical coordinates system $(\vec{x}, \vec{y}, \vec{z})$ (in black) where $\vec{x}$ is oriented towards the North, $\vec{y}$ to the East and $\vec{z}$ pointing downward and the principal stress coordinates system $(\vec{l}, \vec{m}, \vec{n})$ (in blue). The latter coincides with the far-field stresses S_1, S_2, S_3. (c) borehole coordinates system $(\vec{u}, \vec{v}, \vec{w})$. δ and Φ are the borehole azimuth and the borehole inclination respectively. All systems of coordinates are positive orthonormal base. (For interpretation of the references to colour in this figure legend, the reader is referred to the web version of this article.)

In Eq. (C.2), X is an (m x n) matrix containing the inputs excitations, b is a vector of order n, which, we assume, holds the system parameters and c is a vector of order m containing values that describe the system's response to a set of excitations X.

$$X_{p1}b_1 + X_{p2}b_2 + \cdots + X_{pn}b_n = c_p \qquad (C.3)$$

where X_{pi} is the element of X corresponding to the pth row and ith column. As X has m rows, there are m such equations.

The objective function is based on the best set of linear combinations of the parameters b, as affected by the model inputs X, compared to the observations c:

$$\psi = (c - Xb)^t(c - Xb) \qquad (C.4)$$

ψ is the objective function to minimize, c contains the set of laboratory or field measurements; the "t" superscript indicates the matrix transpose operation. It can be shown[18] that the vector b which minimizes ψ of Eq. (C.4) is given by:

$$b = (X^t X)^{-1} X^t c \qquad (C.5)$$

The vector b expressed in Eq. (C.5) is the "best linear unbiased" estimator of the set of true system parameters appearing in Eq. (C.1).

Moreover, two different types of regularization are available in PEST: Singular Value Decomposition (SVD) and Tikhonov regularization[18]. SVD is a method to reduce the process matrices into a smaller number of parameters called subset or "super parameters". This method reduces the null space by dropping parameters that do not affect model outputs. This leads to a computationally less expensive calibration problem. On the other hand, Tikhonov regularization is based on the assumption that the objective function of the inverse problem has two components: one is based on hard knowledge and the other is based on soft knowledge[16]. Detailed discussion of mathematical formulation of regularizations is beyond the scope of this study, but more details can be found in Doherty[16,18].

References

1. Häring MO, Schanz U, Ladner F, Dyer B. Characterisation of the Basel 1 enhanced geothermal system. *Geothermics*. 2008;37(5):469–495. http://dx.doi.org/10.1016/j.geothermics.2008.06.002.
2. Rummel F, Baumgärtner J. Hydraulic fracturing stress measurements in the GPK1 borehole, Soultz-sous-Forêts. *Geothermal Science and Technology*. 1991;3:119–148.
3. Fernández-Ibáñez F, Castillo D, Wyborn D, Hindle D. *Benefits of HT-Hostile Environments on Wellbore Stability: a Case Study from Geothermal Fields in Central Australia*. In Proceedings: Indonesian Petroleum Association; 2009.
4. Alcolea A, Meier P, Vilarrasa V, Olivella S, Carrera J. Induced seismicity assessment of the hydraulic stimulations in borehole PX2 at Pohang (South Korea) using coupled hydromechanical modelling. World geothermal congress 2020, Reykjavik, Iceland, 21-26 May 2020. In: World Geothermal Congress 2020. 2020.
5. Zoback M, Barton C, Brudy M, et al. Determination of stress orientation and magnitude in deep wells. Special issue of the ijrmms: rock stress estimation isrm suggested methods and associated supporting papers; *International Journal of Rock Mechanics and Mining Sciences*. Special issue of the ijrmms: rock stress estimation isrm suggested methods and associated supporting papers; 2003:1049–1076. http://dx.doi.org/10.1016/j.ijrmms.2003.07.001,
6. Zoback MD. *Reservoir Geomechanics*. Cambridge University Press; 2007. http://dx.doi.org/10.1017/CBO9780511586477.
7. Evans K, Meier P. Hydrojacking and hydrofracturing tests in a fissile schist in South-west Switzerland: In-situ stress characterisation in difficult rock. In: Conf. on the Mechanics of Jointed and Faulted Rock, Ed, H.P. Rossmanith, Vienna, April, 1995. 1995.
8. Martin D, Kaiser P, Christiansson R. Stress, instability and design of underground excavations. *International Journal of Rock Mechanics and Mining Sciences*. 2003;40:1027–1047. http://dx.doi.org/10.1016/S1365-1609(03)00110-2.
9. Lin W, Yamamoto K, Ito H, Masago H, Kawamura Y. Estimation of minimum principal stress from an extended leak-off test onboard the chikyu drilling vessel and suggestions for future test procedures. *Scientific Drilling*. 2008;6:43–47. http://dx.doi.org/10.2204/iodp.sd.6.06.2008.
10. Valley B, Evans KF. Stress magnitudes in the Basel enhanced geothermal system. *International Journal of Rock Mechanics and Mining Sciences*. 2019;118(April):1–20. http://dx.doi.org/10.1016/j.ijrmms.2019.03.008.
11. Mastin L, Heinemann B, Krammer A, Fuchs K, Zoback M. Stress orientation in the KTB pilot hole determined from wellbore breakouts. *Scientific Drilling*. 1991;2.
12. Borm G, Engeser B, Hoffers B, Kutter H, Lempp C. Borehole instabilities in the KTB main borehole. 1997. http://dx.doi.org/10.1029/96JB03669.

13. Brudy M, Zoback M. Compressive and tensile failure of boreholes arbitrarily-inclined to principal stress axes: Application to the KTB boreholes, Germany. *International Journal of Rock Mechanics and Mining Sciences*. 1993;30(7):1035–1038. http://dx.doi.org/10.1016/0148-9062(93)90068-O.

14. Chang C, Zoback MD, Khaksar A. Empirical relations between rock strength and physical properties in sedimentary rocks. *Journal of Petroleum Science and Engineering*. 2006;51(3):223–237. http://dx.doi.org/10.1016/j.petrol.2006.01.003.

15. Martin CD, Stimpson B. The effect of sample disturbance on laboratory properties of Lac du Bonnet granite. *Canadian Geotechnical Journal*. 1994;31(5):692–702. http://dx.doi.org/10.1139/t94-081.

16. Doherty J. Ground water model calibration using pilot points and regularization. *Ground Water*. 2003;41:170–177. http://dx.doi.org/10.1111/j.1745-6584.2003.tb02580.x.

17. Alcolea A, Ramírez J, Medina A. Pilot points method incorporating prior information for solving the groundwater flow inverse problem. *Advances in Water Resources*. 2006;29:1678–1689. http://dx.doi.org/10.1016/j.advwatres.2005.12.009.

18. Doherty J. *Calibration and Uncertainty Analysis for Complex Environmental Models*. Blurb, Incorporated; 2015.

19. Kirsch G. Die theorie der elastizitat und die bedurfnisse der festigkeitslehre. *Z Ver Deutscher Ingenieure*. 1898;42:797–807.

20. Carrera J, Alcolea A, Medina A, Hidalgo J, Slooten LJ. Inverse problem in hydrogeology. *Hydrogeology Journal*. 2005;13:206–222. http://dx.doi.org/10.1007/s10040-004-0404-7.

21. Doherty J, Hayes D, Muffels C. PEST home page. URL: https://pesthomepage.org/.

22. Schmitt DR, Currie CA, Zhang L. Crustal stress determination from boreholes and rock cores: Fundamental principles. *Tectonophysics*. 2012:1–26. http://dx.doi.org/10.1016/j.tecto.2012.08.029.

23. Stephens G, Voight B. Hydraulic fracturing theory for conditions of thermal stress. *International Journal of Rock Mechanics and Mining Sciences*. 1982;19(6):279–284. http://dx.doi.org/10.1016/0148-9062(82)91364-X.

24. Terzaghi K, et al. *Erdbaumechanik Auf Bodenphysikalischer Grundlage*. F. Deuticke; 1925.

25. Biot MA. General theory of three dimensional consolidation. *Journal of Applied Physics*. 1941;12(2):155–164. http://dx.doi.org/10.1063/1.1712886.

26. Biot M. The theory of elasticity and consolidation for a porous anisothropic solid. *Journal of Applied Physics*. 1955;26:182–185. http://dx.doi.org/10.1063/1.1721956.

27. Biot M, Willis D. The elastic coefficients of the theory of consolidation. *Journal of Applied Mechanics*. 1957;24:594–601.

28. Zimmerman R. Coupling in poroelasticity and thermoelasticity. *International Journal of Rock Mechanics and Mining Sciences*. 2000;37:79–87. http://dx.doi.org/10.1016/S1365-1609(99)00094-5.

29. Tan X, Konietzky H. Numerical study of variation in Biot's coefficient with respect to microstructure of rocks. *Tectonophysics*. 2014;610:159–171. http://dx.doi.org/10.1016/j.tecto.2013.11.014.

30. Tan X, Konietzky H, Frühwirt T. Experimental and numerical study on evolution of Biot's coefficient during failure process for brittle rocks. *Rock Mechanics and Rock Engineering*. 2015;48(3):1289–1296.

31. Brace W, Martin R. A test of the law of effective stress for crystalline rocks of low porosity. *International Journal of Rock Mechanics and Mining Sciences*. 1968;5(5):415–426. http://dx.doi.org/10.1016/0148-9062(68)90045-4.

32. Suvorov A, Selvadurai A. The Biot coefficient for an elasto-plastic material. *International Journal of Engineering Science*. 2019;145:103166. http://dx.doi.org/10.1016/j.ijengsci.2019.103166.

33. Hajiabdolmajid V, Kaiser P, Martin C. Modelling brittle failure of rock. *International Journal of Rock Mechanics and Mining Sciences*. 2002;39(6):731–741. http://dx.doi.org/10.1016/S1365-1609(02)00051-5.

34. Sahara DP, Schoenball M, Gerolymatou E, Kohl T. Analysis of borehole breakout development using continuum damage mechanics. *International Journal of Rock Mechanics and Mining Sciences*. 2017;97:134–143. http://dx.doi.org/10.1016/j.ijrmms.2017.04.005.

35. Shen B, Stephansson OS, Rinne M. Simulation of borehole breakouts using fracod(2D). *Oil and Gas Science and Technology*. 2002;57:579–590. http://dx.doi.org/10.2516/ogst:2002039.

36. Alcolea A, Kuhlmann U, Marschall P, et al. *A Pragmatic Approach to Abstract the Excavation Damaged Zone Around Tunnels of a Geological Radioactive Waste Repository: Application to the HG-A Experiment in Mont Terri*. Geological Society, London, Special Publications; 2016:SP443.8. http://dx.doi.org/10.1144/SP443.8.

37. Marschall P, Giger S, De La Vassière R, et al. Hydro-mechanical evolution of the EDZ as transport path for radionuclides and gas: insights from the Mont Terri rock laboratory (Switzerland). *Swiss Journal of Geosciences*. 2017;110(1):173–194. http://dx.doi.org/10.1007/s00015-016-0246-z.

38. Coulomb M. Essai sur une application des regles des maximis et minimis a quelquels problemesde statique relatifs, a la architecture. *Memoires de Mathematique Et de Physique, Presentes A L'Academie Royale Des Sciences, Par Diver Savans, &Amp; Lus Dans Let Assemblees. Annee 1773*. 1776:343–382.

39. Mohr O. Welche Umstände bedingen die Elastizitätsgrenze und den Bruch eines Materials. *Z Vereins Deutscher Ingenieure*. 1900;46(1524–1530):1572–1577.

40. Mogi K. Fracture and flow of rocks under high triaxial compression. *Journal of Geophysical Research (1896-1977)*. 1971;76(5):1255–1269. http://dx.doi.org/10.1029/JB076i005p01255.

41. Al-Ajmi AM, Zimmerman RW. The relation between the Mogi and the Coulomb failure criteria. *International Journal of Rock Mechanics and Mining Sciences*. 2005;42.

42. Song I, Haimson BC. Polyaxial strength criteria and their use in estimating in situ stress magnitudes from borehole breakout dimensions. *International Journal of Rock Mechanics and Mining Sciences*. 1997;34(3):116.e1 – 116.e16. http://dx.doi.org/10.1016/S1365-1609(97)00240-2.

43. Ewy R. Wellbore-stability predictions by use of a modified lade criterion. *SPE Drilling and Completion*. 1999;14:85–91. http://dx.doi.org/10.2118/56862-PA.

44. Barton N. The shear strength of rock and rock joints. *International Journal of Rock Mechanics and Mining Sciences*. 1976;13:255–279. http://dx.doi.org/10.1016/0148-9062(76)90003-6.

45. Kwon S, Xie L, Park S, et al. Characterization of 4.2-km-deep fractured granodiorite cores from pohang geothermal reservoir, Korea. *Rock Mechanics and Rock Engineering*. 2019;52(3):771–782. http://dx.doi.org/10.1007/s00603-018-1639-2.

46. Reasenberg PA, Simpson RW. Response of regional seismicity to the static stress change produced by the loma prieta earthquake. *Science*. 1992;255(5052):1687–1690.

47. Iio Y. Frictional coefficient on faults in a seismogenic region inferred from earthquake mechanism solutions. *Journal of Geophysical Research: Solid Earth*. 1997;102(B3):5403–5412. http://dx.doi.org/10.1029/96JB03593.

48. Tanikawa W, Shimamoto T. Comparison of Klinkenberg-corrected gas permeability and water permeability in sedimentary rocks. *International Journal of Rock Mechanics and Mining Sciences*. 2009;46:229–238. http://dx.doi.org/10.1016/j.ijrmms.2008.03.004.

49. Barth N, Boulton C, Carpenter B, Batt G, Toy V. Slip localization on the southern Alpine fault, New Zealand. *Tectonics*. 2013;32(3):620–640.

50. Houston H. Deep earthquakes. 2015:329–354. http://dx.doi.org/10.1016/B978-0-444-53802-4.00079-8,

51. Azzola J, Valley B, Schmittbuhl J, Genter A. Stress characterization and temporal evolution of borehole failure at the Rittershoffen geothermal project. *Solid Earth*. 2019;10(4):1155–1180. http://dx.doi.org/10.5194/se-10-1155-2019.

52. Cuss R, Rutter E, Holloway R. Experimental observations of the mechanics of borehole failure in porous sandstone. *International Journal of Rock Mechanics and Mining Sciences*. 2003;40(5):747–761. http://dx.doi.org/10.1016/S1365-1609(03)00068-6.

53. Diederichs M, Kaiser P, Eberhardt E. Damage initiation and propagation in hard rock during tunnelling and the influence of near-face stress rotation. *International Journal of Rock Mechanics and Mining Sciences*. 2004;41(5):785–812. http://dx.doi.org/10.1016/j.ijrmms.2004.02.003.

54. Walton G, Kalenchuk K, Hume C, Diederichs M. Borehole breakout analysis to determine the in-situ stress state in hard rock. In: ARMA 2015, 49th Us Rock Mechanics / Geomechanics Symposium. 2015.

55. Andersson J, Martin C, Stille H. The Äspö Pillar Stability Experiment: Part II–Rock mass response to coupled excavation-induced and thermal-induced stresses. *International Journal of Rock Mechanics and Mining Sciences*. 2009;46(5):879–895.

56. Hoek E, Martin C. Fracture initiation and propagation in intact rock – A review. *Journal of Rock Mechanics and Geotechnical Engineering*. 2014;6(4):287–300. http://dx.doi.org/10.1016/j.jrmge.2014.06.001.

57. Valley B. And stress heterogeneities in deep-seated crystalline rocks at Soultz-sous-Forêts. 2007.

58. Shen B. Borehole breakouts and in situ stresses. In: First Southern Hemisphere International Rock Mechanics Symposium. 2008, p. 407–18.

59. Shen B, Stephansson O. Modification of the G-criterion for crack propagation subjected to compression. *Engineering Fracture Mechanics*. 1994;47(2):177–189. http://dx.doi.org/10.1016/0013-7944(94)90219-4.

60. Edwards AW. The history of likelihood. *International Statistical Review*. 1974:9–15.

61. De Marsily G. Spatial variability of properties in porous media: A stochastic approach. 1984:719–769. http://dx.doi.org/10.1007/978-94-009-6175-3_15,

62. Kitanidis PK, Vomvoris EG. A geostatistical approach to the inverse problem in groundwater modeling (steady state) and one-dimensional simulations. *Water Resources Research*. 1983;19(3):677–690. http://dx.doi.org/10.1029/WR019i003p00677.

63. Rubin Y, Dagan G. Stochastic identification of transmissivity and effective recharge in steady groundwater flow: 1. Theory. *Water Resources Research Journal*. 1987;23(7):1185–1192. http://dx.doi.org/10.1029/WR023i007p01185.

64. Gutjahr A, Wilson J. Co-kriging for stochastic flow models. *Transport in Porous Media*. 1989;4(6):585–598.

65. Meier PM, Medina A, Carrera J. Geostatistical inversion of cross-hole pumping tests for identifying preferential flow channel within a shear zone. *Ground Water*. 2001;39(1):10.

66. Krige dg. *A Statistical Approach to Some Mine Valuation and Allied Problems on The Witwatersrand*. 1951 URL: https://books.google.ch/books?id=M6jASgAACAAJ.

67. Matheron G. Principles of geostatistics. *Economic Geology*. 1963;58(8):1246–1266. http://dx.doi.org/10.2113/gsecongeo.58.8.1246.

68. Hadamard J. Sur les problèmes aux dérivées partielles et leur signification physique. *Princeton University Bulletin*. 1902:49–52.

69. Tikhonov AN. *Regularization of Incorrectly Posed Problems*. Soviet Mathematics Doklady; 1963.

70. Hendricks-Franssen. Inverse stochastic modelling of groundwater flow and mass transport. 2001.

71. LaVenue AM, Pickens JF. Application of a coupled adjoint sensitivity and kriging approach to calibrate a groundwater flow model. *Water Resources Research Journal*. 1992;28(6):1543–1569. http://dx.doi.org/10.1029/92WR00208.

72. Marquardt DW. An algorithm for least-squares estimation of nonlinear parameters. *The Japan Society for Industrial and Applied Mathematics*. 1963;11(2):431–441.

73. Kaeser B, Kalt A, Borel J. The crystalline basement drilled at the basel-1 geothermal site, a preliminary petrologicalgeochemical study. Report To Geopower Basel AG for Swiss Deep Heat Mining Project Basel. Institut de Géologie Et D'Hydrogéologie, Université de Neuchâtel, Switzerland; 2007.

74. Ziegler M, Valley B, Evans KF. Fault orientations inferred from analysis of a microseismic cluster dataset of the basel EGS reservoir agree well with borehole fracture data. In: *Abstract Volume 13th Swiss Geoscience Meeting, Basel, 20th–21st November 2015: 7. Geothermal Energy, CO2 Sequestration and Shale gas*. Swiss Academy of Sciences; 2015:219.

75. Valley B, Evans KF. Stress orientation to 5 km depth in the basement below Basel (Switzerland) from borehole failure analysis. *Swiss Journal of Geosciences*. 2009;102(3):467–480. http://dx.doi.org/10.1007/s00015-009-1335-z.

76. Deichmann N, Giardini D. Earthquakes induced by the stimulation of an enhanced geothermal system below Basel (Switzerland). *Seismological Research LettersSearch*. 2009;80(5):784–798. http://dx.doi.org/10.1785/gssrl.80.5.784.

77. Valley B, Evans K. Preliminary assessment of the scaling relationships of in-situ stress orientation variations indicated by wellbore failure data. In: Alejano L, Perucho A, Olalla C, Jimémez R, eds. *EUROCK 2014: Rock Engineering and Rock Mechanics: Structures in and on Rock Masses*. CRC Press; 2014.

78. Kastrup U, Zoback ML, Deichmann N, Evans KF, Giardini D, Michael AJ. Stress field variations in the Swiss Alps and the northern Alpine foreland derived from inversion of fault plane solutions. *Journal of Geophysical Research: Solid Earth*. 2004;109(B1). http://dx.doi.org/10.1029/2003jb002550.

79. Kraft T, Deichmann N. High-precision relocation and focal mechanism of the injection-induced seismicity at the Basel EGS. *Geothermics*. 2014. http://dx.doi.org/10.1016/j.geothermics.2014.05.014.

80. Terakawa T, Miller S, Deichmann N. High fluid pressure and triggered earthquakes in the enhanced geothermal system in Basel, Switzerland. *Journal of Geophysical Research*. 2012;117(B7):B07305. http://dx.doi.org/10.1029/2011jb008980.

81. Braun R. *Analyse Gebirgsmechanischer Versagenszustände Beim Geothermieprojekt Basel*. Report to Geopower Basel AG for Swiss Deep Heat Mining Project Basel. Dr. Roland Braun. Consultancy in Rock Mechanics, Basel, Switzerland; 2007.

82. Carrera J, Neuman S. Estimation of aquifer parameters under transient and steady state conditions: 2. Uniqueness, stability, and solution algorithms. *Water Resources Research Journal*. 1986;22:211–227. http://dx.doi.org/10.1029/WR022i002p00211.

83. Akaike H. A new look at the statistical model identification. IEEE Trans Autom Control 19 (6).

84. Akaike H, et al. On entropy maximization principle.. 1977.

85. Rissanen J. Modeling by shortest data description. *Automatica*. 1978;14(5):465–471. http://dx.doi.org/10.1016/0005-1098(78)90005-5.

86. Schwarz G. Estimating the dimension of a model. *Annals of Statistics*. 1978;6:461–464.

87. Hannan EJ. The estimation of the order of an ARMA process. *The Annals of Statistics*. 1980:1071–1081.

88. Kashyap R. Optimal choice of AR and MA parts in autoregressive moving average models. *IEEE Transactions on Pattern Analysis and Machine Intelligence*. 1982;PAMI-4:99–104.

89. Medina A, Carrera J. Geostatistical inversion of coupled problems: dealing with computational burden and different types of data. *Journal of Hydrology*. 2003;281(4):251–264.

90. Barton C, Zoback M, Burns K. In-situ stress orientation and magnitude at the Fenton geothermal site, New Mexico, determined from wellbore breakouts. *Geophysical Research Letters*. 1988;15(5):467–470.

91. Alcolea A, Carrera J, Medina A, et al. A hybrid Marquardt-Simulated Annealing method for solving the groundwater inverse problem. *International Association of Hydrological Sciences*. 2000:157–163.

92. Jaeger J, Cook N, Zimmerman R. *Fundamental of Rock Mechanics*. 2007. http://dx.doi.org/10.1017/CBO9780511735349.

93. Shamir G, Zoback MD. Stress orientation profile to 3.5 km depth near the San Andreas Fault at Cajon Pass, California. *Journal of Geophysical Research: Solid Earth*. 1992;97(B4):5059–5080. http://dx.doi.org/10.1029/91JB02959.

94. Valley B, Evans K. Stress heterogeneity in the granite of the soultz EGS reservoir inferred from analysis of wellbore failure. In: *Proceedings World Geothermal Congress 2010*. 2010 URL: http://www.wgc2010.org/.

95. Afshari Moein MJ, Somogyvári M, Valley B, Jalali M, Loew S, Bayer P. Fracture network characterization using stress-based tomography. *Journal of Geophysical Research: Solid Earth*. 2018;123(11):9324–9340. http://dx.doi.org/10.1029/2018JB016438.

96. Valley B, Evans K. Preliminary assessment of the scaling relationships of in-situ stress orientation variations indicated by wellbore failure data. In: Alejano L, Perucho A, Olalla C, Jimémez R, eds. *EUROCK 2014: Rock Engineering and Rock Mechanics: Structures in and on Rock Masses*. CRC Press; 2014.

97. Schoenball M, Davatzes NC. Quantifying the heterogeneity of the tectonic stress field using borehole data. *Journal of Geophysical Research: Solid Earth*. 2017;122(8):6737–6756. http://dx.doi.org/10.1002/2017JB014370.

98. Holliger K. Upper-crustal seismic velocity heterogeneity as derived from a variety of P-wave sonic logs. *Geophysical Journal International*. 1996;125(3):813–829. http://dx.doi.org/10.1111/j.1365-246X.1996.tb06025.x.

99. Aladejare AE, Wang Y. Evaluation of rock property variability. *Georisk: Assessment and Management of Risk for Engineered Systems and Geohazards*. 2017;11(1):22–41. http://dx.doi.org/10.1080/17499518.2016.1207784.

100. Valley B, Jalali M, Ziegler M, Evans K. Constraining DFN characteristics for deep geothermal projects by considering the effects of fractures on stress variability. In: Proceedings of the 1st International Conference on Discrete Fracture Network Engineering. 2014.

101. Setiawan NB, Zimmerman RW. A unified methodology for computing the stresses around an arbitrarily-shaped hole in isotropic or anisotropic materials. *International Journal of Solids and Structures*. 2020;199:131–143. http://dx.doi.org/10.1016/j.ijsolstr.2020.03.022.

102. Maury, Sauzay, V.M. J. Iadc, s p e and instability, borehole and case, h and mechanics, rock. 1987.

103. Peška P, Zoback MD. Compressive and tensile failure of inclined well bores and determination of in situ stress and rock strength. *Journal of Geophysical Research*. 1995;100(B7):12791. http://dx.doi.org/10.1029/95JB00319.

104. Hiramatsu Y, Oka Y. Determination of the stress in rock unaffected by boreholes or drifts, from measured strains or deformations. *International Journal of Rock Mechanics and Mining Sciences*. 1968;5(4):337–353. http://dx.doi.org/10.1016/0148-9062(68)90005-3.